Journal of Loss Prevention in the Process Industries 99 (2026) 105829

Contents lists available at ScienceDirect

Journal of Loss Prevention in the Process Industries

journal homepage: www.elsevier.com/locate/jlp

A new logarithmic congestion model for vent sizing and reduced pressure prediction in baghouse dust collectors

F. Pinna [a,*], M. Zucca [a], M. Simoncelli [b], F. Stochino [a]

[a] Department of Civil and Environmental Engineering and Architecture, University of Cagliari, Via Marengo 2, Cagliari, 09123, Italy
[b] Department of Architecture, Built Environment and Construction Engineering, Politecnico di Milano, Via G. Ponzio 31, Milano, 20133, Italy

ARTICLE INFO

Keywords:
Blast load
Dust explosion
Dust collectors
Venting standards
Reduced pressure
Blockage ratio obstacle

ABSTRACT

Baghouse dust collectors are recurrent sources of industrial dust explosions, yet current vent-sizing standards (NFPA 68, EN 14491) consistently under-predict the reduced pressure that develops in these highly congested vessels. This study presents a new logarithmic congestion model that incorporates the effect of internal filter volume directly into the classical vent-sizing equation. The correlation is calibrated with a series of full-scale deflagration tests and verified against computational-fluid-dynamics simulations. Compared with the standard NFPA approach, the new model delivers markedly closer agreement with measured reduced pressures across a wide range of dust reactivities and congestion levels. It captures the characteristic behaviour whereby the installation of the first filter rows causes a sharp rise in pressure, followed by a gradual plateau as additional filters are added. By embedding turbulence amplification directly into vent-sizing curves, the model enables realistic prediction of blast loads on collector panels, vent frames, and anchorage systems without resorting to time-consuming CFD. The proposed correlation thus offers loss-prevention engineers a rapid, physically consistent tool for designing explosion-relief systems in baghouse collectors, helping close a long-standing safety gap in the process industries.

1. Introduction

To predict the peak pressure generated by a dust explosion is notoriously difficult in an empty enclosure (Marmo et al., 2025; Islas et al., 2025; Zhang et al. 2024, 2025; Xie et al., 2025), because it depends on flame acceleration, position, geometry, and the initial level of turbulence. A widely adopted strategy to mitigate the effects of confined explosions is the installation of explosion-venting systems. These systems release overpressure to safe areas and thereby limit structural damage and injury risks (Nan et al., 2023; Pang and Liu, 2024; Pang et al., 2023).

Dust explosions represent a critical hazard in industrial environments, capable of causing severe damage to structures, equipment, and endangering human life (U.S. Chemical Safety and Hazard Investigation Board, 2018). When fine combustible particles are dispersed in air within confined volumes, encounter and ignition source, they can trigger rapid combustion events resulting in violent pressure rise and destructive forces. Numerous incidents have been documented since the 18th century (Hassan et al., 2014), and still today dust collectors and storage silos remain among the most recurrent sources of such accidents, as confirmed by recent global surveys (Paltrinieri et al., 2014; Alauddin et al., 2025). Despite the lower ignition sensitivity compared to flammable gases, dust explosions are particularly insidious due to the difficulty of early detection, the persistence of smoldering combustion in hidden compartments, and the complex interaction between flame propagation and internal obstacles or filters (Li et al., 2022). The catastrophic consequences of dust explosions underline the importance of reliable mitigation systems such as explosion venting panels, which aim to limit the maximum internal pressure during deflagration events. As in silos, venting is essential for maintaining vessel integrity during dust explosions (Guan et al., 2025). Similarly, well designed venting systems in dust collectors are not only vital for protecting personnel but also for preserving the structural integrity of industrial facilities. These systems limit peak internal pressures and reduce the dynamic loads transmitted to structural elements during deflagration events. However, as highlighted in the literature, traditional venting standards, (National Fire Protection Association, 2023; European Committee for Standardization, 2012) often struggle to accurately predict the reduced pressure in complex geometries like dust collectors, where internal congestion and

* Corresponding author.
E-mail addresses: francesco.pinna4@unica.it (F. Pinna), marco.zucca2@unica.it (M. Zucca), marco.simoncelli@polimi.it (M. Simoncelli), fstochino@unica.it (F. Stochino).

https://doi.org/10.1016/j.jlp.2025.105829
Received 28 July 2025; Received in revised form 29 September 2025; Accepted 25 October 2025
Available online 27 October 2025

turbulence play a key role in increasing explosion severity (Pinna et al., 2025).

The presence of obstacles significantly increases the severity of turbulent explosions, as their characteristic scale enhances turbulence generation and accelerates combustion, leading to a much steeper rate of pressure rise than predicted by conventional models (Phylaktou et al., 1994). Internal obstacles dramatically intensify turbulence and flame propagation speed, resulting in higher overpressures and multiple pressure peaks. This has been confirmed by the empirical model of Park et al. (2008), which demonstrated that classical correlations tend to underestimate these effects in vented systems with congested geometries. Complex obstacles, such as square rings, further exacerbate the severity of methane or dust explosions by amplifying turbulence and flame speed, producing significantly higher overpressures. Although the use of ultrafine water mist can mitigate these effects, its efficiency remains highly dependent on the geometry and positioning of the obstacles (Xu et al., 2017). Similarly, in vented LPG/air explosions, the presence of internal obstacles drastically intensifies turbulence and explosion severity, generating overpressures and dynamic loads capable of causing severe damage to masonry structures that would otherwise withstand the event in the absence of obstacles (Zhang et al., 2017). In deflagrations involving corn starch dust within combustion ducts, intermediate alter flame propagation, increasing turbulence and combustion pressure. Conversely, very small obstacles tend to inhibit both flame propagation and pressure wave development (Yin et al., 2019). In non-homogeneous methane/air explosions, the obstacle position plays a critical role in amplifying turbulence and explosion severity, with obstacles placed 400 mm from the ignition point generating the highest flame speed and overpressure, resulting in a more violent event compared to uniform conditions (Wu et al., 2022). Even obstacles with low blockage ratios, defined as the ratio between the obstacle area and the cross-sectional area, show a pronounced effect in increasing turbulence, flame speed, and propagation complexity during methane/air explosions. Under these conditions, flame speeds and pressure can increase, demonstrating that even in seemingly uncongested configurations, the influence of obstacles on explosion severity cannot be neglected (Li et al., 2024). In methane/coal dust hybrid explosions, the presence of cubic obstacles amplifies turbulence, flame speed, and peak overpressure. This highlights that, even in dust explosions, the shape and arrangement of obstacles are critical in worsening the severity of the event (Zhou et al., 2024). In summary, both in gas and dust explosions, the presence, shape, arrangement, and positioning of obstacles are key factors that intensify turbulence, accelerate flame propagation, and increase overpressure. These effects are illustrated schematically in Figs. 1 and 2, which depicts how obstacles amplify turbulent flow and flame in confined geometries. These effects are particularly pronounced even in low blockage ratios configurations with or in geometries that might appear only mildly congested, emphasizing the need to account for these aspects when assessing explosion risks in confined or vented environments.

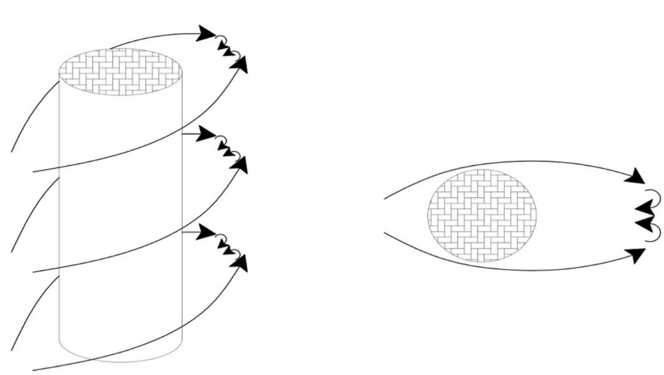

Fig. 1. Turbulent flow structure around a cylindrical filter element obstacle in a confined enclosure. (a) Axonometric view; (b) Planar view. Adapted from Zhou et al. (2024).

This growing body of evidence confirms that, in both gas and dust explosions, the presence, geometry, and positioning of internal obstacles play a pivotal role in intensifying turbulence and accelerating flame propagation factors. As a result, obstacles affect pressure development and often render conventional venting standards to accurately predict explosion severity in congested enclosures such as dust collectors.

As far authors know, structural engineers don't have any quick use formulas or shortcut methods for estimating the reduced explosion pressure, P_{red}, in dust collectors. This absence of expeditive tools makes it difficult to size vents and assess the blast loads that an accident would impose on the collector and nearby structures. Filling this gap is therefore essential and drives motivation for the current study, as it will enable a more informed and safer structural design.

After this brief introduction, the paper is organized as follows. Section 2 presents the experimental data set, nine full scale explosions of vented cartridges filters dust collectors, that provides the basis for model calibration. Section 3 details the numerical simulations carried out with computational fluid dynamic software, CFD, FLACS-DustEx and validated them against the test measurements, achieving agreement on reduced pressure within ±10 %. Section 4 introduces the proposed model, deriving a logarithmic congestion correction that embeds obstacle generated turbulence into classical vent sizing correlations. Section 5 conducts a parametric study with the calibrated model, quantifying how increasing blockage ratio produces a logarithmic rise and to plateau the reduced pressure, P_{red}, and real required vent area, A_{V0}. Finally, Section 6 summarizes the main findings, outlines design implications and applicability limits, and recommends priorities for future research, including additional full-scale tests with highly reactive dust and configurations equipped with ducted vents.

2. Experimental data

As far as the authors are aware, the only publication study campaigns that combine realistic filter congestion, well-instrumented venting, and multiple dust chemistries are those carried out by Lunn and Cairns (1985) and Lunn et al. (1998). In their experiments, sketched in Figs. 3 and 4, tested various dust types such as polyethylene, phenolic resin, toner, maize starch, and anthraquinone under different configurations of vent location, filter, and ignition timing. A key focus was whether the explosion was effectively confined to the "dirty volume", V_{Dirty}, (i.e., hopper and the filter region directly exposed to dust) or whether it also involved "clean" compartments, which could become dusty depending on the actual operating conditions.

Lunn and Cairns (1985) installed six pressures transducers, three on the dirty side and three on the clean side of the commercial dust collectors so that over pressure on both compartments could be recorded simultaneously during normal filtration and reverse air cleaning. Although the exact sensor model was not reported, the results of the reduced pressure values, P_{red}, were as follows in Table 1:

Lunn et al. (1998) employed TransInstruments Type 2000 G A gauges, sampled at 1 kHz for channel via a Microlink 3000 data acquisition unit and processed with FAMOS software. The reduced pressure values, P_{red}, observed in the tests are as follows in Tables 2 and 3:

In Tables 4–8, the main dust properties and geometric characteristics of the tested configurations, including the filters volume to dirty volume ratio, $V_{Filters}/V_{Dirty}$. In all experiments, the vent panels were equipped with static activation pressure, P_{stat}, fixed at 10 kPa.

The experiments of Lunn and Cairns Lunn and Cairns (1985) first validate the FLACS-DustEx computational fluid dynamics, CFD, model, while the nine full-scale tests presented here then provide the benchmark data set used in Section 4 to calibrate the proposed logarithmic congestion model. This sequential validation-and-calibration approach underpins the subsequent analysis of how changes in blockage ratio

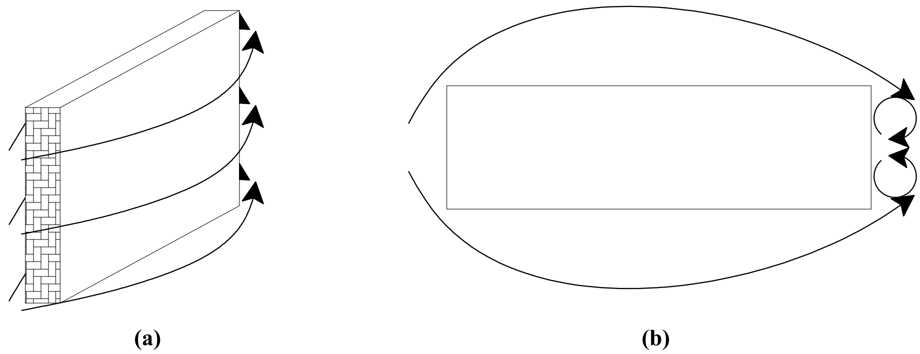

Fig. 2. Turbulent flow structure around a square filter element obstacle in a confined enclosure. (a) Axonometric view; (b) Planar view. Adapted from Zhou et al. (2024).

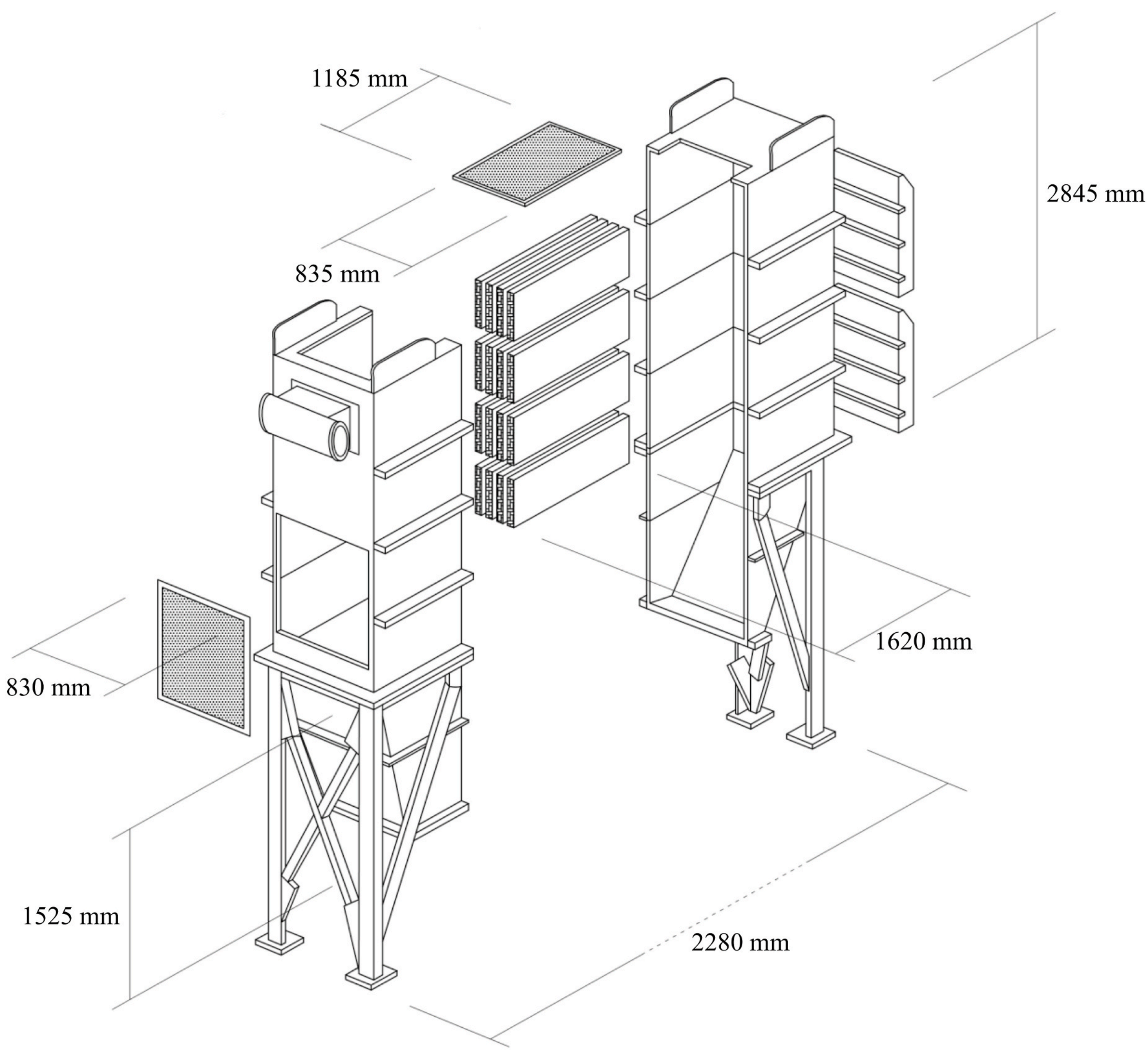

Fig. 3. Exploded view of dust collector showing square filter elements and vent panel integration adapted from Lunn and Cairns (1985).

affect the reduced explosion pressure, P_{red}.

3. Numerical simulations

Several studies have demonstrated that FLACS is a validated and reliable tool for predicting reduced pressure, P_{red}, resulting from vent opening, as it accurately models the flame acceleration phase and the discharge dynamics in congested enclosures Li and Hao (2017); Hansen et al., 2010a,b; Ma et al., 2014; Hansen et al., 2010a,b; Skjold et al. (2005); Tascón and Aguado (2017); Arntzen et al. (2025); Pang et al. (2022); Skjold (2007); Lyu et al. (2024); Skjold et al. (2005); Li et al. (2023); Li et al. (2025).

In the present section, three representatives full scale experiments were simulated, with v 25.1 of FLACS-DustEx, to provide an

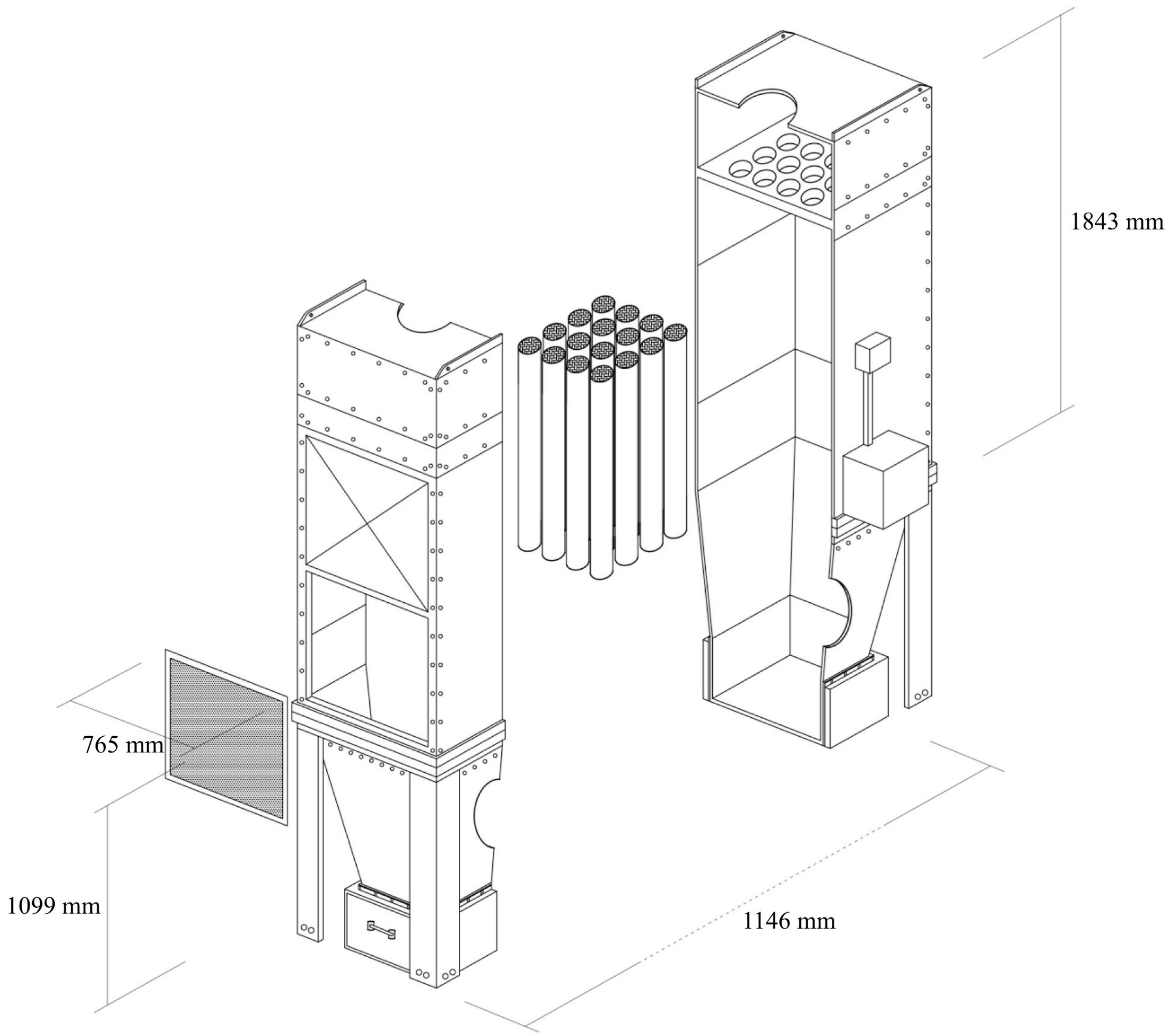

Fig. 4. Exploded view of dust collector showing cylindrical filter elements and vent panel integration adapted from Lunn et al. (1998).

Table 1
Experimental observations for the P_{red} in dust collector of Lunn and Cairns (1985).

Dust	$P_{red,exp}$ [kPa]
Polyethylene	14
Phenolic Resin	2
Toner	9
Aspirin	14

Table 2
Experimental observations for the P_{red} in dust collector, UMA 250, of Lunn et al. (1998).

Dust	$P_{red,exp}$ [kPa]
Maize Starch	11
Anthraquinone	16
Toner	12

independent validation benchmark.

Dust reactivity parameters $(P_{\max}, K_{st})$ were taken from the experimental database of Lunn and Cairns (1985). Particle size and cloud concentration used in CFD were set exactly as reported in Tables 4 and 5,

Table 3
Experimental observations for the P_{red} in dust collector, UMA 750, of Lunn et al. (1998).

Dust	$P_{red,exp}$ [kPa]
Toner	12
Anthraquinone	11

Table 4
Properties of the dust measured in a 20-L reported in Lunn and Cairns (1985).

Dust	P_{max} [kPa]	K_{St} [MPa m/s]	$(dP/dt)_{max}$ [MPa/s]	Particle modal size class [μm]	Concentration [kg/m^3]
Polyethylene	721	13.8	50.8	10-20 (70.7 %)	0.50
Phenolicresin	667	14.0	51.6	>160 (34.0 %)	3.00
Toner	752	16.9	62.3	10-20 (50.3 %)	0.50
Aspirin	775	19.0	70.1	36-56 (22.7 %)	1.50

Table 5
Properties of the dust measured in a 20-L reported in Lunn et al. (1998).

Dust	Pmax [kPa]	KSt [MPa m/s]	(dP/dt)$_{max}$ [MPa/s]	Particle modal size class [μm]	Concentration [kg/m^3]
Maize Starch	800	14.0	52	n.r.	0.450–0.900
Anthraquinone	800	31.8	82	n.r.	0.225–0.500
Toner	710	22.2	117	n.r.	0.250–0.930

Table 6
Geometric characteristics of the dust collector, and their vent used during the experiments in Lunn and Cairns (1985).

Dirty Volume [m^3]	Area Top Vent [m^2]	Area Side Vent [m^2]	Area Total Vent [m^2]	$V_{Filters}/V_{Dirty}$
4.23	0.99	0.71	1.70	0.6

Table 7
Geometric characteristics of the dust collector, UMA 250, and their vent used during the experiments in Lunn et al. (1998).

Dirty Volume [m^3]	Effective Area Vent [m^2]	Area Total Vent [m^2]	$V_{Filters}/V_{Dirty}$
0.67	0.28	0.55	0.5

Table 8
Geometric characteristics of the dust collector, UMA 750, and their vent used during the experiments in Lunn et al. (1998).

Dirty Volume [m^3]	Effective Area Vent [m^2]	Area Total Vent [m^2]	$V_{Filters}/V_{Dirty}$
2.36	0.63	1.23	0.4

the modal particle-size class and the in-vessel concentration corresponding to the maximum K_{st} in the 20-L tests. Because Lunn et al. (1998) do not report particle-size information for the collector trials, the independent CFD validation in this work is restricted to Lunn and Cairns (1985) to ensure full transparency and reproducibility of the input parameters. A homogeneous ignition of 10 kJ was applied at the dust cloud.

In accordance with Lunn and Cairns (1985), the vent was modelled as a PTFE membrane (0.2 mm) pop-out panel with nominal static burst pressure $P_{stat} = 10$ kPa and geometric vent area equal to the experimental configuration reported in Table 6. In FLACS-DustEx this is implemented as a pressure-triggered opening: when the local panel pressure reaches P_{stat}, the boundary switches from closed to open and the effective opening grows to the full area A_v with a short, prescribed opening time (light membrane; negligible inertia/hinge friction).

Each simulation was matched to the Lunn and Cairns (1985) tests in which the dust cloud was artificially re-suspended immediately prior to ignition, yielding a near-uniform suspension comparable to 20-L vessel conditions. This represents a conservative worst-case for P_{red}. To broaden the validation benchmarks, we compared the simulated pressure histories against the records from the first three internal transducers (T1–T3).

All six outer faces were set to Euler/open boundary conditions to allow unrestricted venting. The enclosure was initially filled with quiescent air at 20 °C and 1 bar with zero initial turbulence. This choice mirrors the Lunn and Cairns (1985) protocol, where a uniformly suspended dust cloud was produced (including a series with artificially injected dispersion into the hopper) and the air was brought to rest before ignition; we therefore initialized a quiescent, fully suspended cloud (zero background turbulence) to ensure a like-for-like, conservative validation.

The computational fluid dynamics (CFD) domain consisted of a 1.0 m × 4.0 m × 5.4 m core resolved with a uniform cell size $\Delta = 0.05$ m; outside the region of interest the mesh was smoothly expanded (stretching factor 1.30) to a 5.5 m × 12 m × 6.5 m outer domain to suppress spurious reflections while keeping the Courant number within limits. This base resolution, selected in accordance with FLACS-DustEx best-practice guidance for vented deflagrations in congested enclosures, provides adequate discretization of the key geometrical scales, yielding ≥ 10 cells across the vent aperture, and ≥ 5 across the filter-row pitch, and roughly 80–100 cells along the principal flame-acceleration path. Experimental data was acquired at 1 kHz. For the St-1/St-2 cases considered here, the dominant rise spans 0.2–0.4 s, so this rate resolves the timing. However, finite sampling and the necessary pre-differentiation smoothing attenuate peak dp/dt, which we report as a conservative value. The CFD solver advances with an adaptive internal step ($CFL = \frac{\Delta t}{\Delta x} \leq 0.5$) but is exported at $\Delta t = 0.001$ s to match the data. We note that very fast transients typical of St-3 dusts were not part of the present validation and may require higher sampling rates. The final grid comprised 7.5×10^5 cells with aspect ratio ≤ 1 in the core. A targeted mesh-sensitivity check (one coarser and one finer level) confirmed adequacy of the chosen grid: the peak reduced pressure and the rise timing remained effectively unchanged within engineering tolerance.

Simulations were performed on a 20 thread Intel i7-13650HX workstation, with 32 GB DDR5, RTX 4060 8 GB. Simulations for the lower K_{St} powders required approximately 36 h to reach convergence, while those with a higher K_{St} value completed in about 18 h. Fig. 5 compares the experimental pressure time records (black) with the simulated traces (red) for polyethylene dust (transducer 1, T1, in Lunn and Cairns, 1985), aspirin dust (transducer 2, T2, in Lunn and Cairns, 1985) and polyethylene dust (transducer 3, T3, in Lunn and Cairns, 1985).

Fig. 6 shows a representative example of the rate of pressure rise comparison dp/dt for T1 obtained from the same signals, while Fig. 7 reports simulated overpressure contours at selected times at the transducer locations of Fig. 5. In all cases the peak reduced pressure is reproduced within ±10 %, indicating that the selected mesh resolution, combustion settings and vent-panel model are adequate for engineering predictions. For the rate of pressure rise analysis, using an homemade MATLAB code, experimental and CFD traces were deduplicated and resampled onto a common 500 Hz grid, interpolated with Piecewise Cubic Hermite Interpolating Polynomial (Fritsch and Carlson, 1980), smoothed with a third-order Savitzky–Golay filter (Schafer, 2011) with 11-sample window, and differentiated by a central difference operator. The rise window was defined from the first exceedance of the baseline noise (mean + 3σ over the initial 100 ms) to the time of the experimental peak. Within this window we report the peak dp/dt, the time-to-peak offset and the RMSE. The results, reported in Table 9, show that the timing of the rise is captured to within a few 10 ms, whereas the peak dp/dt is conservatively estimated to be consistent with the simplified vent-opening model and with the necessary pre-differentiation smoothing.

In the case of the Polyethylene, T3, the peak pressure stays close to the vent set-point ($P_{stat} = 0.1$ bar g), so the panel did not fully open. The rise is therefore very gentle and dp/dt is small (Experiment data, EXP ≈ 0.9 kPa/s), with the CFD giving a conservative yet negligible value. Despite the small dp/dt, the primary observable P_{red} is still matched within ±10 %.

3.1. Relationship between filter congestion and reduced pressure

Once the CFD model had been validated against the experimental full-scale tests, it was employed to quantify how the ratio between the filter volume, $V_{Filters}$, and the dirty volume, V_{Dirty}, changes the reduced explosion pressure P_{red}. Fig. 8 illustrates the dust collector geometry adopted in the CFD simulations; the four cartridge rows are color coded

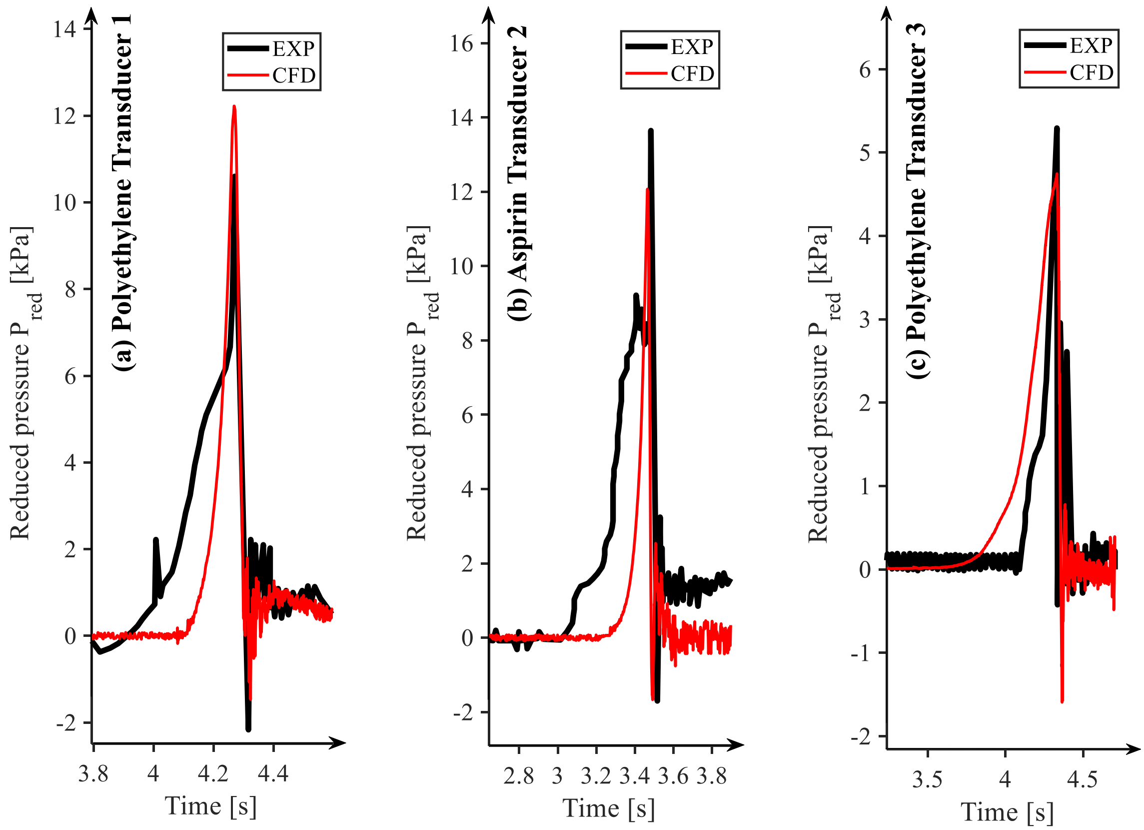

Fig. 5. Comparison of experimental and FLACS-DustEx, CFD, simulated pressure–time profiles for dust collector explosions with: (a) polyethylene dust, transducer 1; (b) aspirin dust, transducer 2; (c) polyethylene dust, transducer 3. The black curve represents the experimental data in Lunn and Cairns (1985), while the red curve depicts the FLACS-DustEx, CFD, simulation. (For interpretation of the references to color in this figure legend, the reader is referred to the Web version of this article.)

green, orange and magenta to show the blockage levels investigated:

- Case A: Green, orange, and magenta rows are present, corresponding to $V_{Filters}/V_{Dirty} = 0.6$.
- Case B: Orange row removed, corresponding to $V_{Filters}/\ V_{Dirty} = 0.45$.
- Case C: Orange, and magenta rows removed, corresponding to $V_{Filters}/V_{Dirty} = 0.3$.
- Case D: Green, orange, and magenta rows removed, corresponding to $V_{Filters}/V_{Dirty} = 0.0$.

These four cases were chosen so that congestion could be varied by sequentially removing entire cartridge rows (top–down), ensuring a controlled and monotonic change in $V_{\text{Filters}}/V_{\text{Dirty}}$ and avoiding artefacts from non-physical removal orders. For these reasons predictions outside this range (x < 0.30) are extrapolations and should be used with caution.

For geometrical configurations were each combined with two carbohydrate dusts of identical chemical properties, 500 g/m^3, and $P_{max} =$ 860 kPa but different K_{St}, the first has 150 bar m/s and the second 300 bar m/s. The red marker (MP) denotes the monitoring point at which the pressure-time histories were recorded. This location was selected because preliminary numerical simulations carried out to validate the CFD model showed that it is where the highest internal overpressures develop.

Figs. 9 and 10 compare the pressure time histories obtained for the four blockage ratios. In both cases the peak pressure grows rapidly when the first row of cartridges is added, but the increment diminishes as additional rows are introduced. The response therefore follows a logarithmic trend, a steep initial rise driven by the sudden increase in turbulence and flame acceleration, followed by a progressive saturation as the flow approaches the choking limits imposed by the vent area and the finite combustion rate. Figs. 9 and 10 show that the presence of internal obstacles consistently raises the reduced explosion pressure, confirming that obstacle congestion amplifies blast severity for both slow to moderate dust (15 MPa/s $\leq K_{St} <$ 30 MPa/s) and fast dust ($K_{St} \geq$ 30 MPa/s). The post vent oscillations exhibit the same order of magnitude, with the most congested case, $V_{Filters}/V_{Dirty} = 0.60$, showing only marginally higher residual pulsations than the intermediate $V_{Filters}/V_{Dirty} = 0.45$ and $V_{Filters}/V_{Dirty} = 0.30$ scenarios.

Fig. 11 summarizes the outcomes of the eight computational fluid dynamics, CFD, simulations by plotting the reduced pressure, P_{red}, against the blockage volume ratio $V_{Filters}/V_{Dirty}$. The peak pressures observed in the pressure–time histories of Figs. 9 and 10 were used to determine the reduced pressure corresponding to each blockage ratio. The plot distinguishes between low reactivity dust ($K_{St} \leq 30\ MPa\ m\ /s$) and high reactivity dust, ($K_{St} > 30\ MPa\ m\ /s$).

Classical venting models relate the reduced pressure to a competition between combustion and vent discharge, at example $P_{red} \propto \Phi\left(K_{St}, A_v^{eff}, V, P_{stat}\right)$, where A_v^{eff} is an effective area accounting for transient opening and losses. Internal obstacles raise turbulence intensity u' and shorten the combustion scale, which can be expressed as an effective deflagration index:

$$K_{St}^{eff} = K_{St}[1 + \alpha \ln(1 + \beta x)] \quad (1)$$

With congestion ratio $x = V_{Filters}/V_{Dirty}$ capturing obstacle-induced turbulence amplification and its eventual saturation. Substituting K_{St}^{eff} into the venting balance yields:

$$P_{red} \propto \Phi\left(K_{St}[1 + \alpha \ln(1 + \beta x)], A_v^{eff}, V, P_{stat}\right) \quad (2)$$

Following standard correlations for premixed turbulent flame, extended in the dust literature for measurement and K_{st} based estimates

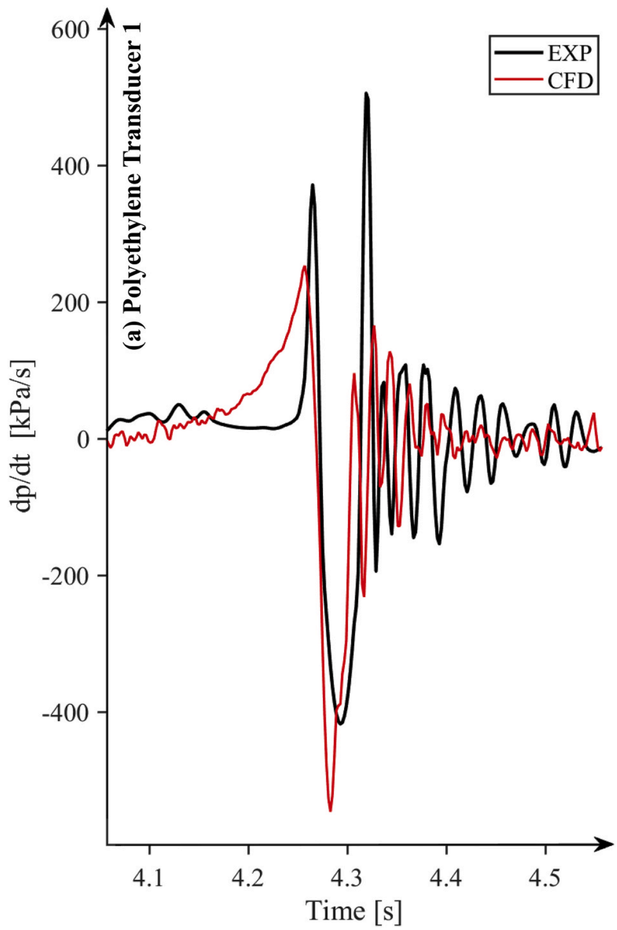

Fig. 6. Rate-of-pressure-rise comparison $dp/dt(t)$ for Polyethylene, Transducer 1 (T1). The black curve represents the experimental data in Lunn and Cairns (1985), while the red curve depicts the FLACS-DustEx, CFD, simulation. (For interpretation of the references to color in this figure legend, the reader is referred to the Web version of this article.)

we can write the ratio between the turbulent burning velocity S_T to the laminar burning velocity S_L as a function of the turbulence intensity (Bradley et al., 2013):

$$\frac{S_T}{S_L} = f\left(\frac{u'}{S_L}\right) \tag{3}$$

The increment due to obstacles is multiplicative in the baseline reactivity. For fast dust, with larger K_{St}/S_L the term $u'/\ S_L$ produces a larger fractional increase in S_T and thus in K_{St}^{eff}, leading to a steeper P_{red}.

To clarify the phenomenon just discussed, we reported the peak reduced pressures P_{red} from the cases shown in Figs. 9 and 10, in Fig. 11, fitted P_{red} to the congestion ratio $x = V_{\text{Filters}}/V_{\text{Dirty}}$ using a logarithmic model:

$$P_{red} = \delta \cdot \ln\left(1 + \frac{V_{Filters}}{V_{Dirty}}\right) + b \tag{4}$$

Where α and β are empirical model parameters. α quantities turbulence sensitivity, and β is a dust-dependent coefficient. Fitting Eq. (4) to the data gives, for the low-reactivity class, $\delta = 2.32$ kPa and $b = 11.73$ kPa, and for the fast class $\delta = 5.80$ kPa and $b = 15.69$ kPa, here δ measures how sensitively P_{red} increases with congestion. This expression accurately captures the observed nonlinear trend: a sharp increase in P_{red} at low blockage levels due to enhanced turbulence and flame acceleration, followed by a slower growth as the effect of additional obstacles saturates.

In summary, the validated CFD simulations reveal a clear logarithmic relationship between reduced pressure and blockage ratio, $V_{Filters}/V_{Dirty}$. This trend indicates that the effect of internal obstacles, such as filters, can be embedded into vent sizing correlations through a logarithmic correction term. This forms the basis of the model developed in Section 4.

4. Proposed model

Because the current vent sizing standard predicts reduced pressure, P_{red}, without accounting for internal obstacles such as filters in dust collectors Pinna et al. (2025), this paper presents a modified equation that explicitly represents their effect. Considering the evidence gathered from full-scale experiments and validated CFD simulations, a logarithmic correction is proposed to account for the influence of internal congestion. The new formulation extends the classical model by adding a logarithmic correction term that represents the volume and arrangement of the internal filters. This enhanced approach provides a more reliable estimation of the maximum pressure developed during a vented dust explosion in geometrically complex systems. In line with the standard and historical literature (VDI 3673, 2002; Eckhoff, 2003; Abbasi and Abbasi, 2007; Cashdollar, 2000), it is important to note that the proposed correlation must be used with pressure values expressed in gauge bar (bar g), as the empirical coefficients in the equation have been specifically calibrated for these units. However, for consistency with global reporting practices, all numerical results presented in this study are converted into the International System (SI) units of kilopascal (kPa) and, where appropriate, megapascal (MPa).

The corrected equation is expressed as follows:

$$A_{V0,NEW} = C \cdot \frac{P_{max} \cdot K_{St}\left[1 + \alpha \ln\left(1 + \beta_{St}\frac{V_{Filters}}{V_{Dirty}}\right)\right] \cdot V_{Dirty}^{\frac{3}{4}}}{P_{red}^{\gamma}} \tag{5}$$

Where.

- $C = 3.264 \cdot 10^{-5}$ is a constant retained from the original historical correlation, NFPA 68, (2023) ensuring consistency with the classical vent sizing curves.
- A_{V0} is the vent area [m^2].
- P_{stat} is the nominal static burst pressure of the vent [bar g].
- K_{St} is the deflagration index [bar m/s].
- P_{max} is the maximum pressure developed in an unvented explosion [bar g].
- P_{red} is the reduced pressure after deflagration venting [bar g].
- α is the turbulence sensitivity coefficient.
- β_{St} is the dust class coefficient. $\beta_{St,slow}$ is for slow to moderate dust with $K_{St} \leq 300$ bar m/s. $\beta_{St,fast}$ for fast dust with $K_{St} > 300$ bar m/s.
- γ is the polytropic index.
- $V_{Filters}$ is the volume of filter elements inside the collector.
- V_{Dirty} is the volume of the dirty side of the collector.

Equation (2) is valid within the parameter range covered by the full-scale experiments used for calibration.

– 7.1 bar g $\leq P_{\text{max}} \leq$ 8.0 bar g.
– 138 bar m/s $\leq K_{\text{St}} \leq$ 318 bar m/s.
– 0.28 m$^3 \leq V_{Dirty} \leq$ 4.23 m^3.
- $P_{\text{stat}} = 0.1$ bar g.
- $L/D = H/D_{\text{he}} = 1$. Where is L or H the distance from the ignition point to the vent, and D or D_{he} is the equivalent diameter of the container.
- $0.4 \leq \frac{V_{Filters}}{V_{Dirty}} \leq 0.6$.

The classical deflagration index, K_{St}, is calculated in empty vessels, calculated using American Society for Testing and Materials. (2020),

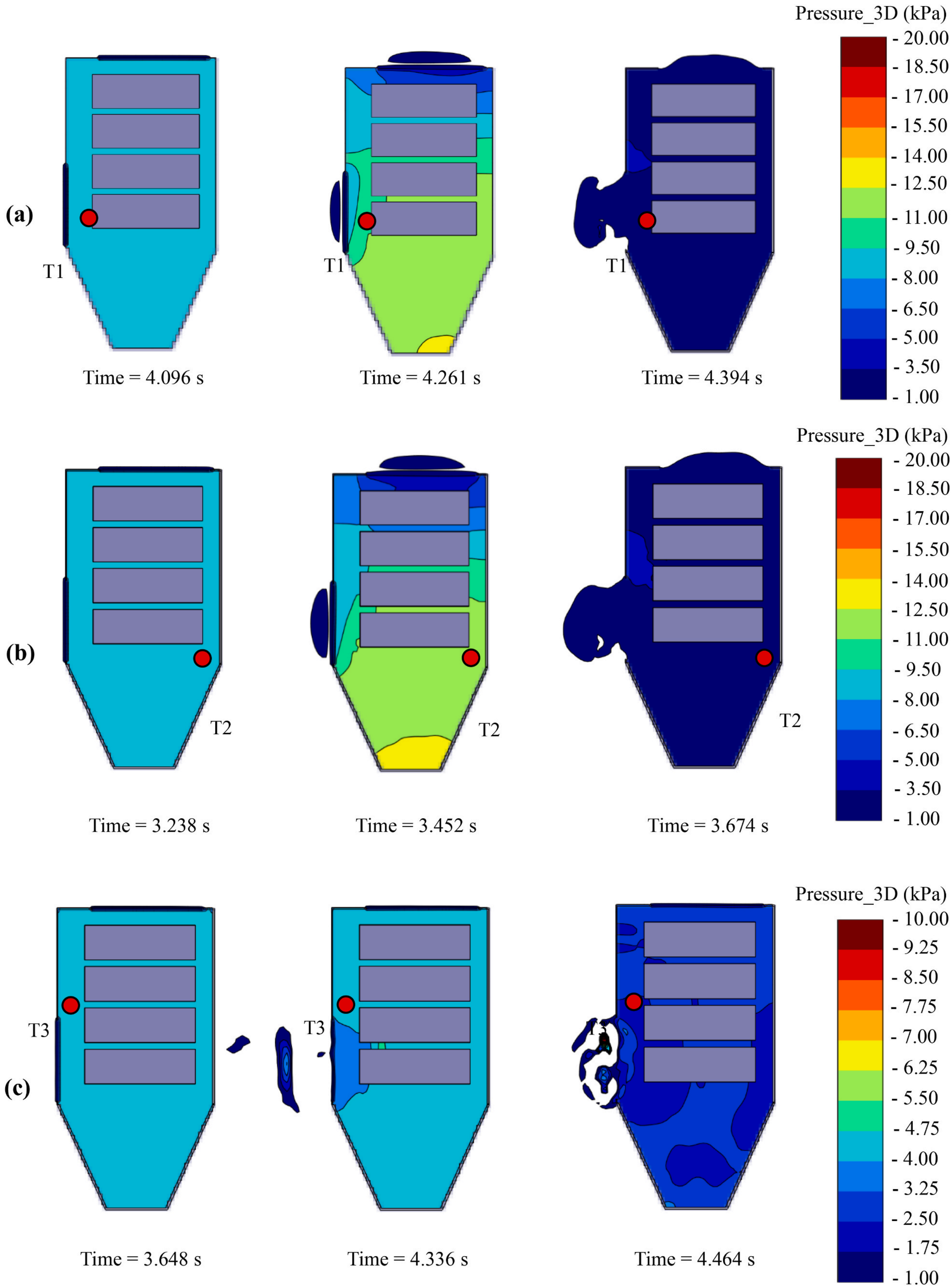

Fig. 7. Contour plots of overpressure in the dust collector section at selected time steps from FLACS-DustEx, CFD, simulations: (a) polyethylene dust, transducer 1; (b) aspirin dust, transducer 2; (c) polyethylene dust, transducer 3. The red dots indicate the locations where pressure was monitored to produce the time history curves shown in Fig. 5. (For interpretation of the references to color in this figure legend, the reader is referred to the Web version of this article.)

Table 9
Summary of rate-of-pressure-rise (dp/dt) validation metrics for the three full-scale cases.

Test	$(dP/dt)_{max}$ EXP [kPa/s]	$(dP/dt)_{max}$ CFD [MPa/s]	Δt [s]	RMSE [kPa/s]
Polyethylene, T1	334.1	247.8	−0.01	69.3
Aspirin, T2	556.6	244.2	−0.02	225.5
Polyethylene, T3	0.9	0.3	−0.08	0.2

and thus establishes not into account any internal congestion. The experimental test used to the K_{St} established those classes already hinted that flame acceleration is highly related to turbulence and consequently obstacles. Subsequent obstacle studies confirmed two robust facts. First, for slow and moderate dust the first row of baffles or filter cartridges can treble the flame tip speed and raise the peak over pressure (Bartknecht, 1981). Second, once the dust cloud is already fast, upper $K_{St} > 300$ bar m/s, the same hardware yields only marginal gains and may even depress combustion when local quenching or sonic choking sets in (Skjold, 2018; Amyotte et al., 1988). These observations rule out any linear or power-law scaling; what is needed is a curve that climbs rapidly at first and then rolls off toward a ceiling.

To evaluate the congestion level, the x ratio is introduced as follows:

$$x = \frac{V_{Filters}}{V_{Dirty}} \tag{6}$$

Where $0 \leq x < 1$ and with $V_{Filters} > 0$ and $V_{Dirty} \geq 0$. The ratio x is unity-free and collapses to $x = 0$ when the collector is empty. Given previously described trends a logarithmic function is used to amplify the x ratio:

$$f(x) = 1 + \alpha \ln(1 + \beta_{St} \cdot x) \tag{7}$$

Where α, and β_{St} are the congestion parameters that need to be tuned. This proposal modulates the K_{St} index through a logarithmic amplifi-

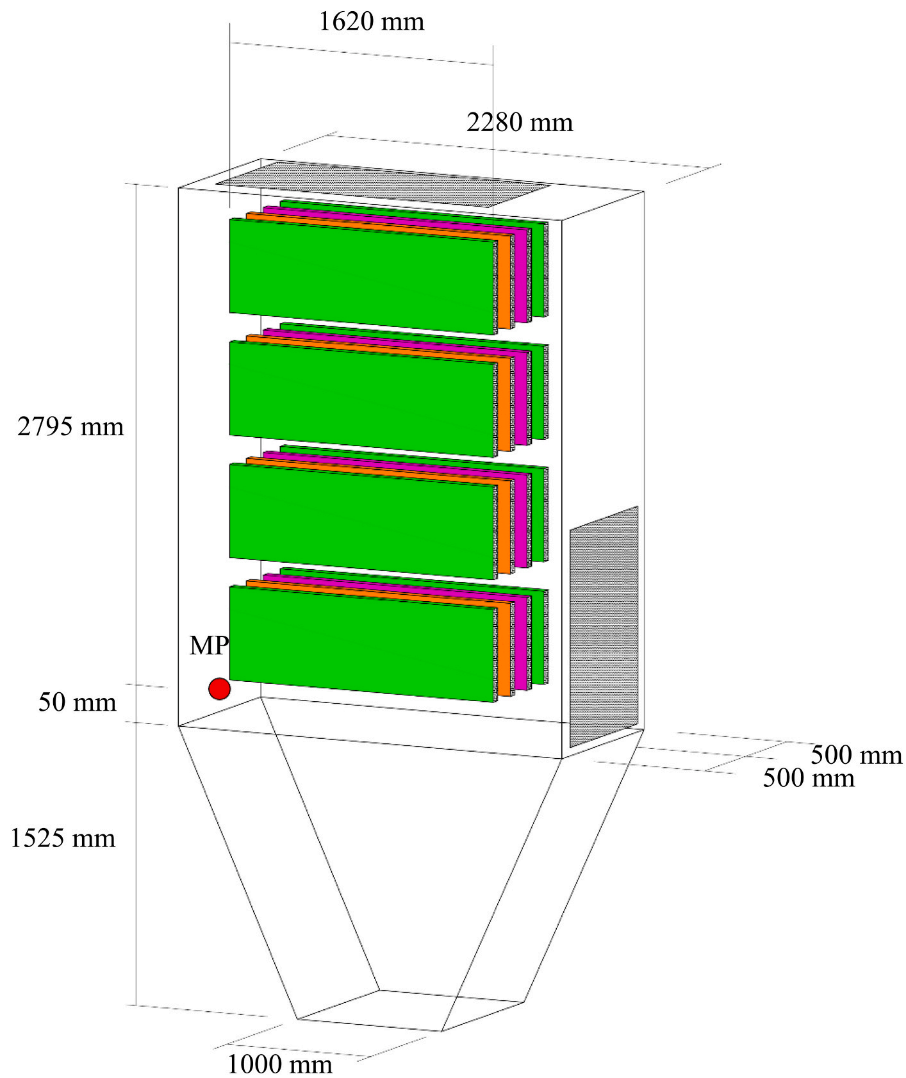

Fig. 8. Geometry of dust collector used in the CFD model, based on the configuration reported in Lunn and Cairns (1985). The colored cartridge rows represent the difference between levels investigated. Case A: all four rows remained (green, orange, magenta); Case B: orange row removed; Case C: orange and magenta rows removed; Case D: orange, magenta and green rows removed. The red marker (MP) denotes the monitoring point where pressure time histories were recorded for all simulations. (For interpretation of the references to color in this figure legend, the reader is referred to the Web version of this article.)

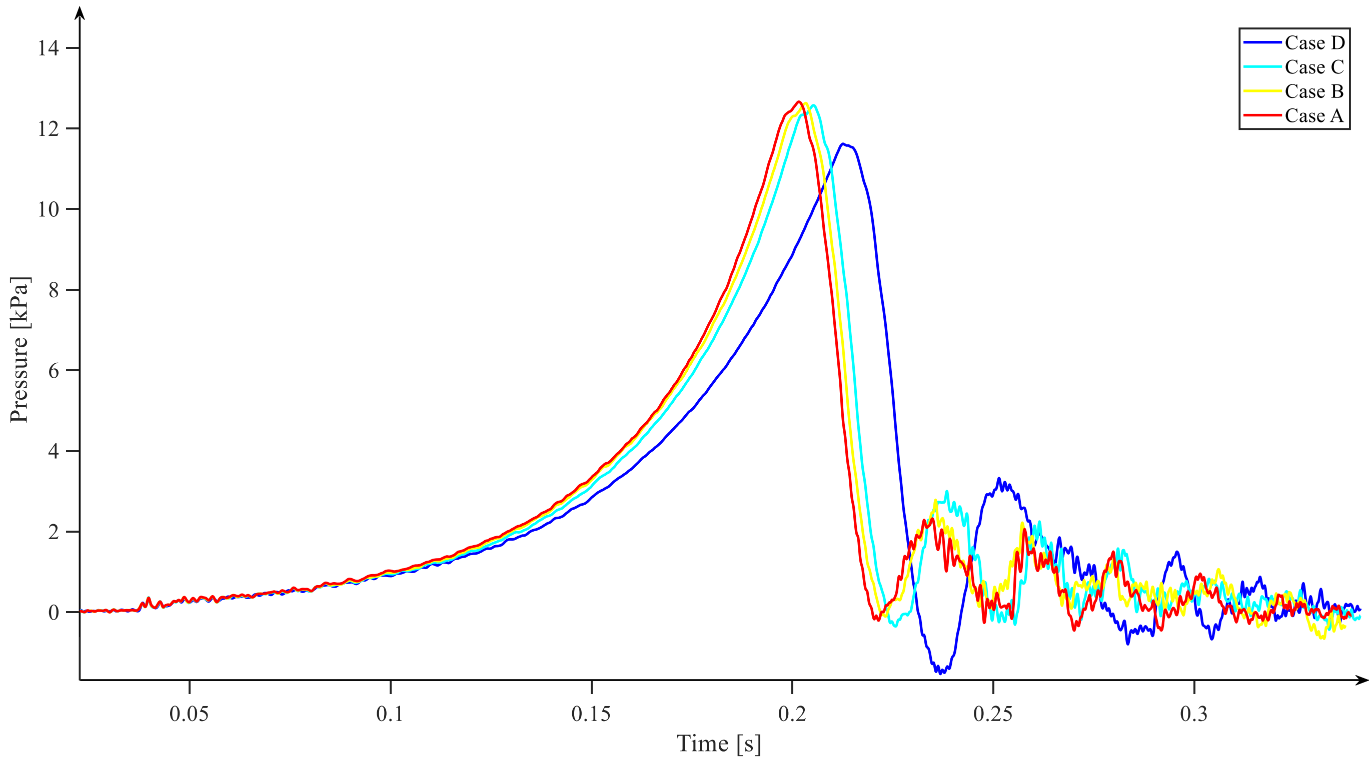

Fig. 9. Pressure-time histories for four different congestion ratios $V_{Filters}/V_{Dirty}$ under blast loading, generated from tests with a dust of deflagration index $K_{St} = 15$ MPa m/s. The traces correspond to configurations with congestion ratios of 0.0 (blue), 0.30 (cyan), 0.45 (yellow), and 0.60 (red), highlighting the influence of filter density on the dynamic pressure response. (For interpretation of the references to color in this figure legend, the reader is referred to the Web version of this article.)

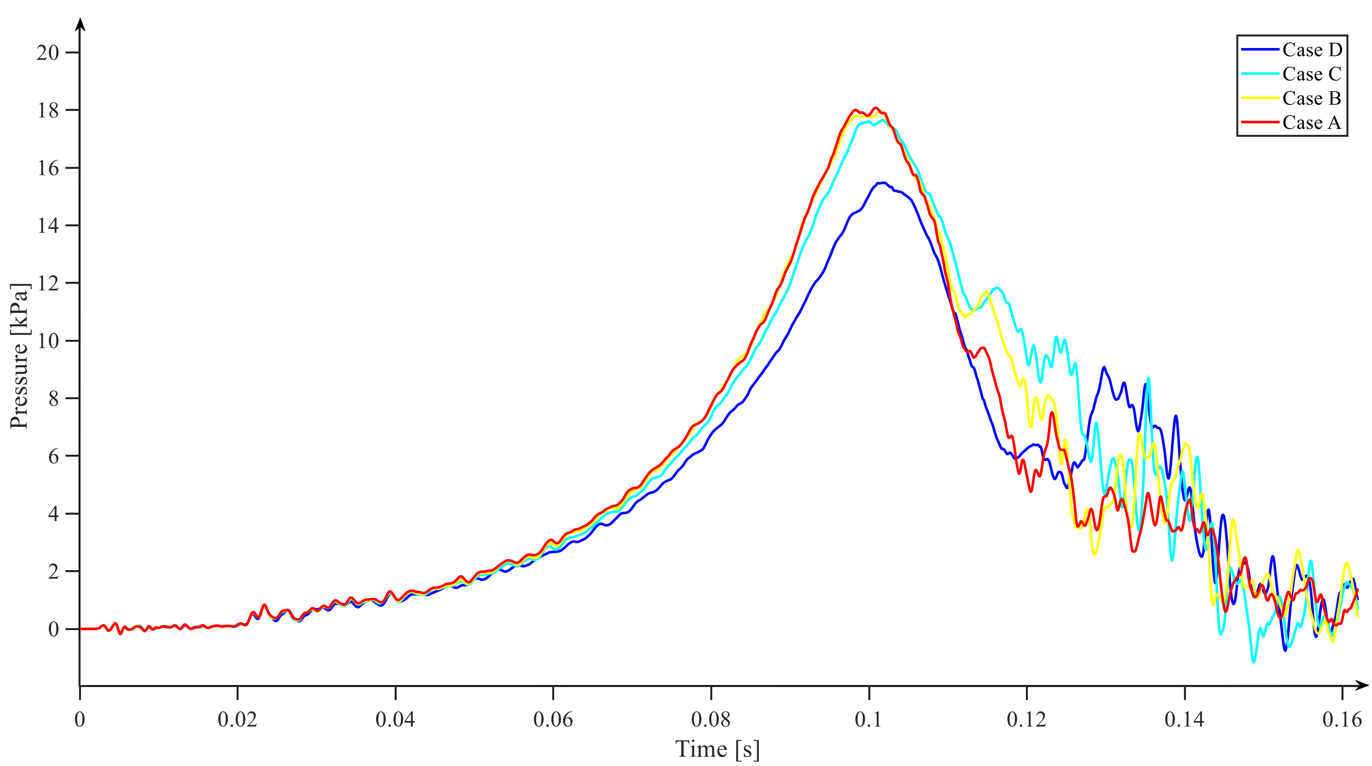

Fig. 10. Pressure-time histories for four different congestion ratios $V_{Filters}/V_{Dirty}$ under blast loading, generated from tests with a dust of deflagration index $K_{St} = 30$ MPa m/s. he traces correspond to configurations with congestion ratios of 0.0 (blue), 0.30 (cyan), 0.45 (yellow), and 0.60 (red), highlighting the influence of filter density on the dynamic pressure response. (For interpretation of the references to color in this figure legend, the reader is referred to the Web version of this article.)

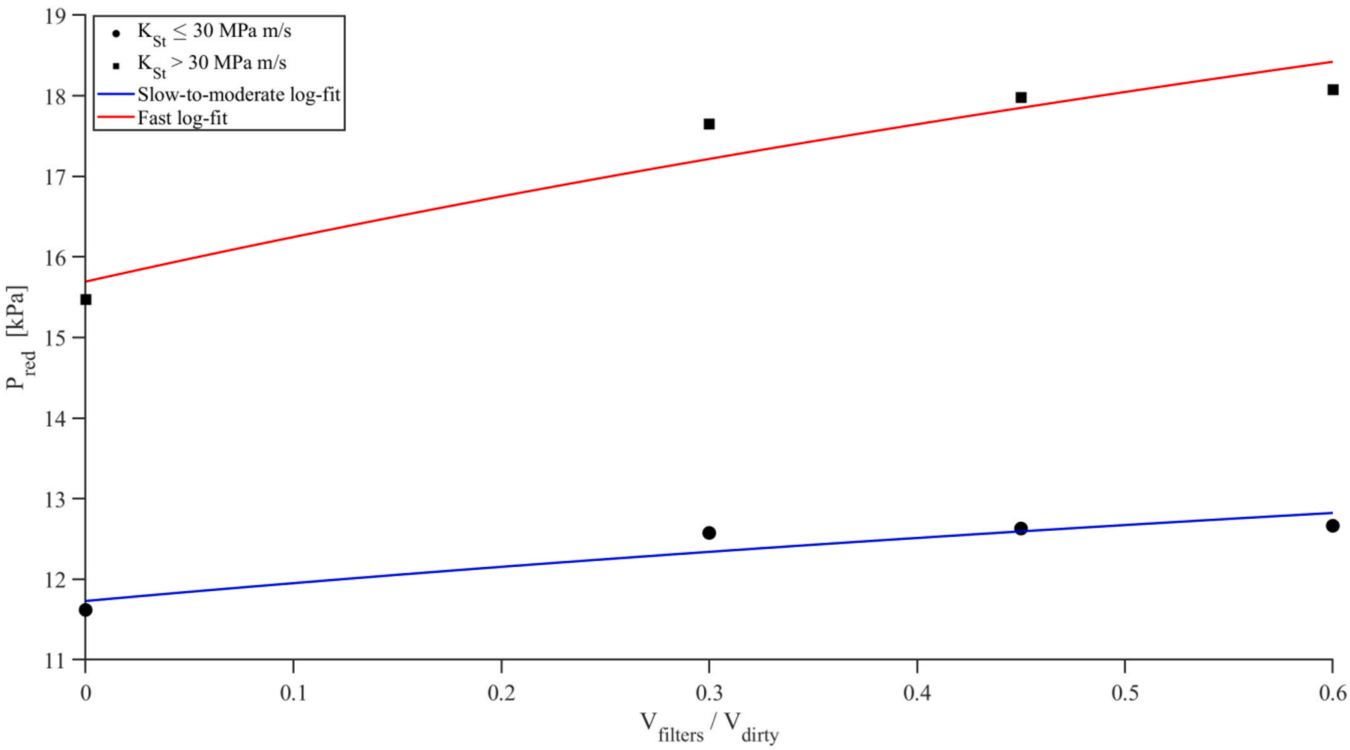

Fig. 11. Reduce pressure, P_{red}, as a function of the blockage volume ratio $V_{Filters}/V_{Dirty}$ for two dust reactivity classes. Black circles and squares represent experimental data for low and high reactivity, respectively. The blue and red curves are logarithmic fits showing a stronger pressure increase with congestion for highly reactive dust. (For interpretation of the references to color in this figure legend, the reader is referred to the Web version of this article.)

cation.

Differentiating with respect to the obstacle volume gives:

$$\frac{\partial f(x)}{\partial V_{Filters}} = \frac{\partial}{\partial V_{Filters}}\left[1 + \alpha \cdot \ln\left(1 + \beta_{St} \cdot \frac{V_{Filters}}{V_{Dirty}}\right)\right] = \alpha \cdot \frac{\beta_{St}}{1 + \beta_{St} \cdot x} \frac{1}{V_{Dirty}} \quad (8)$$

So, every additional obstacle volume, like filters, enlarges the required vent area. In this way the denominator $(1 + \beta_{St} \cdot x)$ grows linearly, forcing the slope to decay; the incremental benefit df/dx thus inevitably tends to zero.

At the opposite extreme, $x \rightarrow 1^{-}$, the logarithm converges to a finite limit that represents the maximum turbulence intensification attainable before flow choking and thermos diffusive saturation arrest further flame acceleration.

4.1. Physical interpretation of the logarithmic congestion factor

The logarithmic congestion factor presents in Equation (5) describes rapid rise followed by a saturation profile of the P_{red}. Its derivative $(1/x)$ presents higher values for small x, flattering at larger values.

Furthermore, the constant β_{St} represents the reactivity of the dust and therefore must be tuned differently for slow and for fast clouds. Following a classification like the historical monographs (Bartknecht, 1978) two K_{St} classes are introduced. Specifically, there is a threshold of 300 bar m/s to better distinguish between slow and moderate reacting dust and fast reacting dust:

- Slow to moderate dusts ($K_{St} \leq 300$ bar m/s): $\beta_{St} = \beta_{St,slow}$
- Fast dusts ($K_{St} > 300$ bar m/s): $\beta_{St} = \beta_{St,fast}$

The different physical behavior between the two regimes requires distinct values of β_{St}.

For $K_{St} \leq 300$ bar m/s dust clouds the laminar burning velocity is modest. Obstacles and narrow passages create intense shear layers that roll up into eddies (Zhou et al., 2024). Solid particles, being orders of magnitude denser than the air, cannot immediately follow the rapidly changing flow and therefore experience large slip velocities. Once the local turbulent layer exceeds the capture threshold, particles are entrained into the core of the eddies where oxygen is plentiful. The more the burning surface the higher the flame tip variation is. Multiplies the burning surface and can treble the flame tip speed. The fitted coefficient $\beta_{St,slow}$ therefore takes a comparatively large value so that $f(x)$. Upper K_{St} > 300 bar m/s dust already possess vigorous turbulence generation mechanisms in the absence of obstacles. Additional roughness cannot raise the flame speed indefinitely because two fundamental constraints are encountered.

The first is the aerodynamic choking. In a compressible flow the mass flux through a restriction attains a maximum when the local Mach number reaches unity (Robert et al., 1984):

$$\dot{m}_{max} = \mu \cdot A \cdot P_0 \sqrt{\frac{\vartheta}{R \cdot T_0}} \cdot \left(\frac{2}{\vartheta + 1}\right)^{\frac{\vartheta+1}{2\cdot(\vartheta-1)}} \quad (9)$$

Where $\dot{m}_{max}$ is the maximum mass flow rate, μ is the discharge coefficient, A is the throat area, P_0 and T_0, respectively, are the upstream pressure and temperature, ϑ is the ratio of specific heats, and R is the specific gas constant. Although originally developed for ideal gases, the chocked flow Equation (6) is commonly adopted in explosion venting models to estimate the maximum mass flux through vent openings, even in dust air suspensions (Eckhoff, 2003; Abbasi and Abbasi, 2007; Bauwens et al., 2010). This represents a simplification, as the multiphase nature of dust clouds is not explicitly considered. Beyond this point the upstream flow becomes decoupled from downstream pressure waves; enhancing turbulence downstream of the choke can no longer accelerate the dust/air column ahead of the flame.

The second is the thermo diffusive saturation. The burning rate of an individual particle is ultimately bound by its own diffusion time scale and local stoichiometry Peters (2001). Extra folding of the flame surface through turbulence wrinkles does not translate into proportional mass

Table 10
Summary of experimental conditions and measured reduced explosion pressures observed in full scaled vented test on dust collectors, presented in Lunn and Cairns (1985) and Lunn et al. (1998).

Vent area, A_{V0} [m^2]	Dirty volume, V_{Dirty} [m^3]	Filter congestion ratio, $V_{Filters}/V_{Dirty}$ [/]	Maximum Pressure, P_{max} [kPa]	Deflagration index, K_{St} [MPa m/s]	Experimental reduced pressure, $P_{red,exp}$ [kPa]
0.28–1.7	0.672–4.23	0.4–0.6	710–800	13.8–31.8	2–16.1

Table 11
Calibrated model parameters for the proposed vent sizing and reduced pressure equation.

α	$\beta_{St,slow}$	$\beta_{St,fast}$	γ
$9.3752 \cdot 10^4$	$+1.0755 \cdot 10^{-5}$	$-8.6434 \cdot 10^{-6}$	0.87268

consumption once the limit is reached. These mechanisms flatten or even slightly reduce the pressure build up, particularly in highly reactive clouds. The logarithmic correction term describes this physical behavior by allowing the congestion factor to plateau or taper off at high K_{St} values, reflecting the limited effectiveness of turbulence enhancement in such scenarios.

4.2. Parameters calibration

To calibrate the proposed logarithmic correlation for vent area in dust collectors, we compared its predictions against full scale explosion experiments reported by Lunn and Cairns (1985) and Lunn et al. (1998). These studies represent the only known experimental campaigns conducted on commercial dust collectors operating under realistic filtration conditions, without additional ducts or auxiliary components (Pinna et al., 2025). The reliability of these tests, conducted in 1985 and 1998, has been further reinforced through CFD simulations in Section 3. This validation approach strengthens the credibility of the dataset and supports its use as a benchmark for model assessment.

Calibration of the congestion parameters, α, β_{St}, and γ parameters rely on the nine full scale vented explosion tests carried out Lunn and Cairns (1985) and Lunn et al. (1998), on three industrial dust collectors. The dataset extension is reported in Table 10:

The pressure transducers employed in the original campaigns declared an accuracy of ± 0.02 bar g, which provides a practical lower bound to the attainable fitting error. Equation (5) was algebraically inverted so that the reduced pressure, P_{red}, became dependent variable:

$$P_{red} = \left[C \cdot \frac{P_{max} \cdot K_{St} \left[1 + \alpha \ln \left(1 + \beta_{St} \frac{V_{Filters}}{V_{Dirty}} \right) \right] \cdot V_{Dirty}^{\frac{3}{4}}}{A_{V0}} \right]^{\frac{1}{\gamma}} \quad (10)$$

And the piecewise definition:

$$\beta_{St} = \begin{cases} \beta_{St,slow} & K_{St} < 300\ bar\frac{m}{s} \\ \beta_{St,fast} & K_{St} \geq 300\ bar\frac{m}{s} \end{cases}$$

For clarity, β_{st} is the same dimensionless congestion-scaling coefficient is used throughout Equation (5). The parameters vector is therefore $\mathbf{p} = \{\alpha, \beta_{St,slow}, \beta_{St,fast}, \gamma\}$. α is unconstrained on $\mathbb{R}$, $\beta_{St} > -\frac{V_{Filters}}{V_{Dirty}}$ for the logarithmic function definition and $\gamma > 0$ in order to have an inverse relationship between P_{red} and A_{V0}. The unknowns were determined by minimizing the root mean square error (RMSE) between calculated ($P_{red,calc}$) and experimental ($P_{red,exp}$) reduced pressures:

$$RMSE(\mathbf{p}) = \sqrt{\frac{1}{N}\sum_{i=1}^{N}\left(P_{red,calc,i}[\mathbf{p}] - P_{red,exp,i}[\mathbf{p}]\right)^2} \quad (11)$$

Complementary performance is quantified by the mean absolute error (MAE):

$$MAE(\mathbf{p}) = \frac{1}{N}\sum_{i=1}^{N}\left|P_{red,calc,i}[\mathbf{p}] - P_{red,exp,i}[\mathbf{p}]\right| \quad (12)$$

Where N is the number of full-scale experimental test. Because Equation (7) is nonlinear, the problem was solved with the Nelder-Mead algorithm (Luersen and Le Riche, 2004; Zahara and Kao, 2009), develop, in MATLAB environment. The algorithm starting from $\mathbf{p_0}$ a random value, convergence tolerances were set to 10^{-6} for the parameters and 10^{-9} for the cost function, with limits of 10^4 iterations and 2 x 10^4 function evaluations. The optimized coefficients are reported in Table 11.

A point-by-point comparison between the experimental, $P_{red,exp}$, and the proposed model results, $P_{red,calc}$, is given in Table 11. For the sake of clariness, the corresponding reduced pressures calculated from the standard NFPA 68 equations, $P_{red,NFPA}$ as reported in Pinna et al. (2025), have also been included for reference. The logarithmic congestion parameters markedly improve agreement for the more heavily congested configurations, as evident from the side-by-side comparison in Table 12.

Table 13 summarizes the residual statistics, see Equations (8) and (9), reproduced here for clarity.

Overall, the congestion parameters calibrated on this limited data-

Table 12
Experimental reduced pressure values, P_{red}, obtained during full scale dust collector explosions compared to predictions from the proposed model, and from the NFPA 68 standard.

Dust Collector	Dust	$P_{red,exp}$ [kPa]	$P_{red,calc}$ [kPa]	$P_{red,NFPA}$ [kPa]
Lunn et al. (1998) (UMA 250)	Maize starch	11	11	0.3
Lunn et al. (1998) (UMA 250)	Toner	16.1	16.2	0.7
Lunn et al. (1998) (UMA 250)	Antraquinone	12	9.7	1.6
Lunn and Cairns (1985)	Polyethylene	14	6.4	0.4
Lunn and Cairns (1985)	Phenolic resin	2	5.9	0.4
Lunn and Cairns (1985)	Toner	9	8.4	0.7
Lunn and Cairns (1985)	Aspirin	14.0	10	0.9
Lunn et al. (1998) (UMA 750)	Toner	12.4	17.4	0.9
Lunn et al. (1998) (UMA 750)	Antraquinone	10.7	13	2.2

Table 13
Summary of residual statistics and model performance indicators for the nine-test calibration dataset.

Item	Comment
Number of tests = 9	This is a limited dataset, each individual test significantly affects the averages. The residual patterns thus require qualitative inspection, in addition to the numerical diagnostics reported below.
RMSE = 3.7 kPa MAE = 2.8 kPa	Because designers use P_{red}, the value of (approximately 4 kPa) is about twice the stated accuracy of the pressure transducers (±2 kPa) and can be considered acceptable for engineering level predictions. The mean absolute deviation lies just 45 % above the experimental background and remains well below 3 kPa.
Mean residual = $\bar{r}$ = $\frac{1}{N}\sum_{i=1}^{N}\left(P_{red,calc,i} - P_{red,exp,i}\right) = +0.3$ kPa	Practically the mean residual. Over and under predictions cancel out across the nine experiments.
Residual standard deviation = s_r = $\sqrt{\frac{1}{N-1}\sum_{i=1}^{N}(r_i - \bar{r})^2} = 3.9$ kPa	Very close to the RMSE, confirming that random scatter dominates the error distribution, with no significant systematic drift.
Residual range: 5 kPa ⇆ +7 kPa	Extreme deviations are still $< \pm 8$ kPa, symmetrical enough to push mean residual to
$\gamma = 0.87268$ (forced >0)	With this γ, the model now introduces a mild super linear curvature. This is physically plausible if pressure amplification accelerates faster than proportional under the combined influence of P_{max}, K_{St} and congestion parameters.

base reproduces the pressure response of cartridge equipped dust collectors within the bounds of experimental uncertainty, without introducing detectable bias errors between slow and fast burning dusts. The improved reliability of the predicted reduced pressure P_{red}, enhances both safety assessments and parametric studies aimed at ranking the influence of internal congestion. The error statistics sit comfortably within the expected measurement uncertainty and mirror the limited variability of the test matrix. Moreover, the absence of bias and the symmetric residual range show that the piecewise β_{St} reconciles slow and fast burning powders without favoring either group. Although derived from only nine experiments, the resulting fit remains robust enough for first-tier design work or for parametric studies where capturing systematic trends matters more than point-wise precision.

5. Parametric study

This section uses the logarithmic proposed model developed in Section 4 to examine how the blockage volume ratio, $V_{Filters}/V_{Dirty}$, alters the vent area needed for a given explosion scenario and the reduced pressure, that develops once the panel opens. The analysis keeps the dust collector geometry documented by Lunn and Cairns (1985). The objective is to demonstrate that the proposed correlation not only reproduces the benchmark results but also represents the logarithmic increase in explosion severity as congestion increases. Although the regression coefficients were calibrated using data in the range $0.40 \leq x \leq 0.60$, additional simulations were performed for $x < 0.40$ to assess the model's behavior when extrapolated beyond the calibration domain. Unless otherwise stated, the $P_{max} = 860$ kPa, $K_{St} = 30$ MPa m/s, and the reference vent panel area in the baseline configurations is $A_{V,0} = 1.70$ m^2. The analysis is limited to dusts with a deflagration index $K_{St} \leq 30$ MPa m/s, since only two of the nine full-scale experiments exceeded this value, providing insufficient evidence to support reliable extrapolation beyond this threshold.

Fig. 12 plots the required vent area as a function of the effective deflagration index, for congestion ratios from $x = 0.00$ to $x = 0.60$. For an obstructed plenum the correlation collapses near to the NFPA 68 vent-sizing line (dashed black), confirming consistency when no turbulence enhancing obstacles are present. Fig. 12 shows the result of the

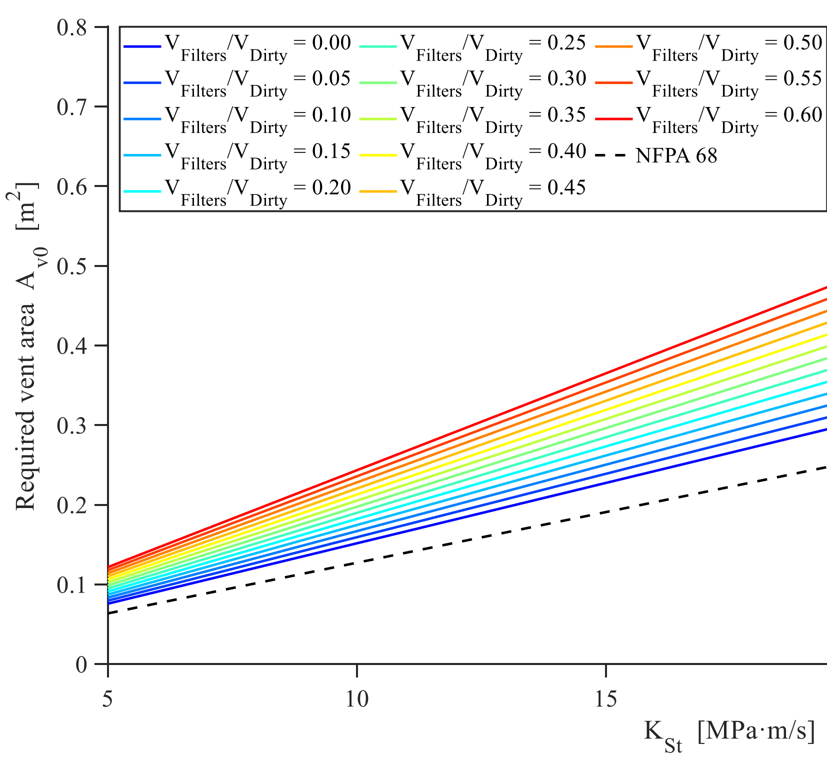

Fig. 12. Required vent area, $A_{V,0}$, versus effective deflagration index K_{St} for $V_{Filters}/V_{Dirty} = 0.00$ to $V_{Filters}/V_{Dirty} = 0.60$. The proposed correlation converges with the NFPA 68 vent sizing in the absence of internal obstruction.

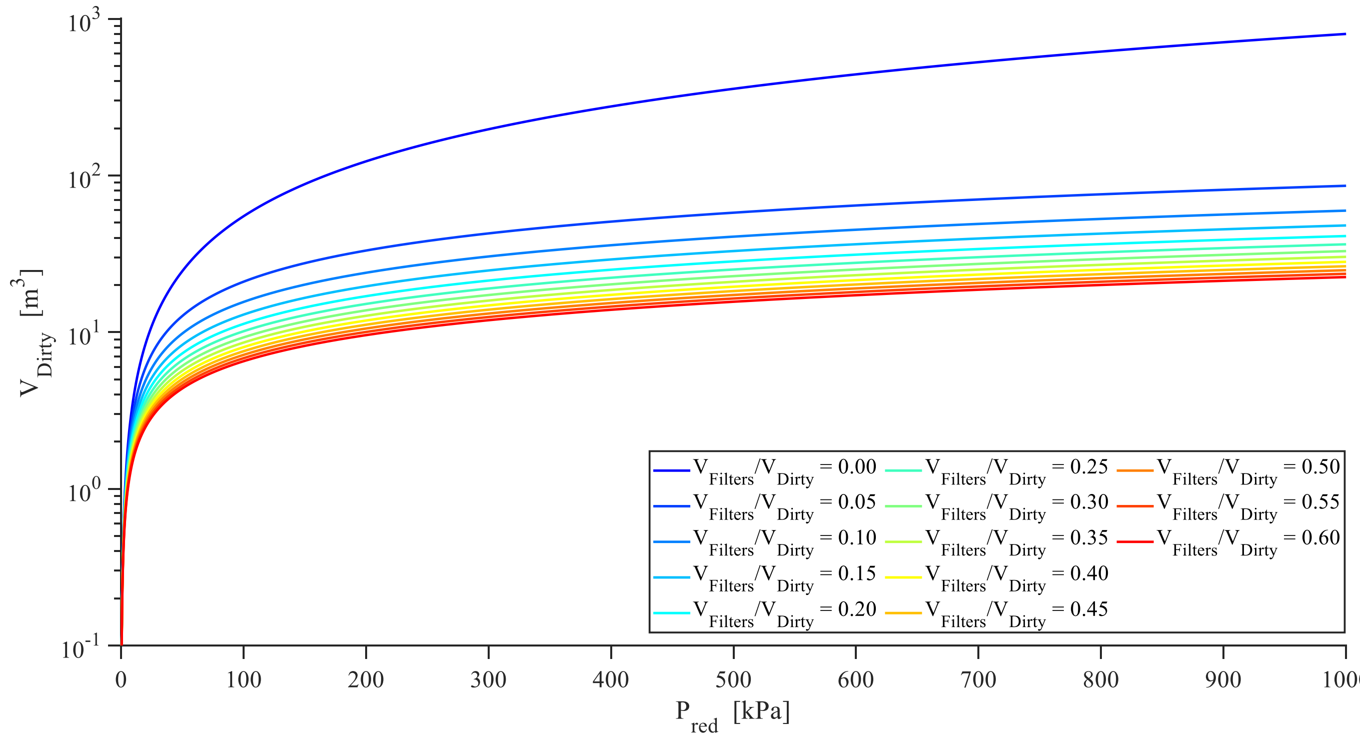

Fig. 13. Maximum protectable dirty side volume V_{Dirty} as a function of reduced explosion pressure, P_{red}, for fixed vent area, $A_{V,0} = 1.7\ m^2$. Each curve represents a different $V_{Filters}/V_{Dirty}$.

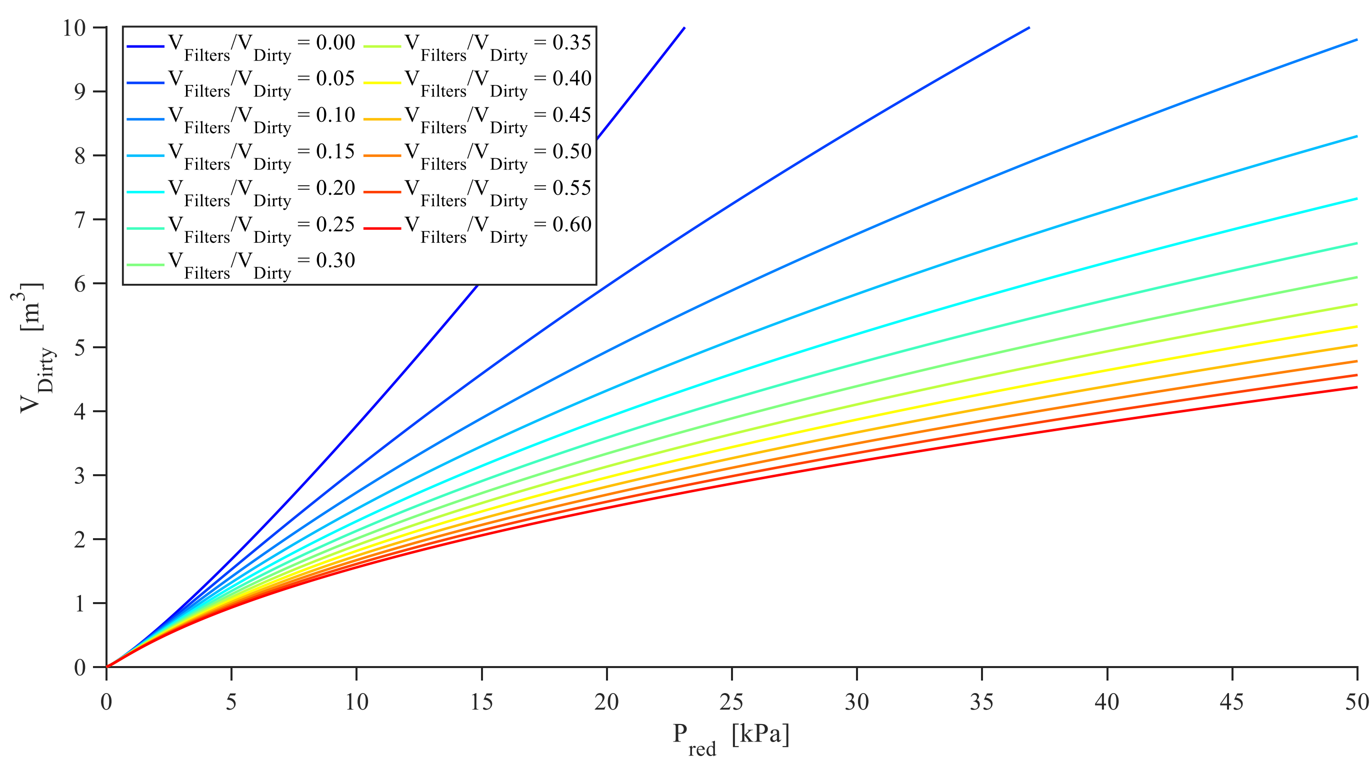

Fig. 14. Zoom in on the design range with $P_{red} < 50$ kPa, typically specified by filter manufacturers to prevent mechanical damage to cartridge frames. Linear axes aid interpolation for practical collector sizes.

re-arranged Equation (10) to express the dirty, V_{Dirty}, volume that can be protected as a function of the design P_{red} for a fixed vent area. For a given reduced pressure, the allowable volume shrinks rapidly from $x = 0.00$ to $x = 0.20$, following a plateau. Designers can therefore exploit the graph as a nomogram starting from the V_{Dirty}, then intersecting the target P_{red}, on the x-axis with the appropriate $V_{Filters}/V_{Dirty}$ curve. Fig. 14 zooms in on the practical design range $P_{red} < 50$ kPa. This is the pressure window typically used by filter manufacturers to avoid structural damage to the cartridge frames. These parametric charts transform the calibrated correlation into a design tool that keeps the simplicity of classic nomograms, reported in Bartknecht (1978), while embedding the congestion effects demonstrated experimentally and numerically in Fig. 13.

6. Conclusions and future perspectives

This study introduced a physically based correction to classical vent sizing models by a logarithmic factor that accounts for internal turbulence enhancing obstacles in dust collectors. The proposed formulation was calibrated against nine full-scale experimental explosions and validated through dedicated CFD simulations, demonstrating its capability to reproduce reduced pressures with good agreement across a range of dust reactivities and geometrical configurations. The model can represent the rapid escalation of explosion severity at low to moderate congestion ratios and correctly predicts the tendency to plateau as the obstacle volume increases.

The analysis demonstrates that the congestion ratio, $V_{Filters}/V_{Dirty}$, is a key parameter governing the pressure amplification in vented dust collectors. Within the tested range, the model reliably reproduces experimental pressures and highlights the physical transition from turbulence driven escalation to saturation, a behavior not captured by current standards such as NFPA 68 or EN 14491. At present, no other model can estimate the reduced pressure, P_{red}, in dust collectors with comparable accuracy. For structural engineers, having even a first order estimate of the maximum reduced pressure is important to preliminary sizing of anchorage systems and determine whether dust collectors should be located away from primary structural elements or outside the building envelope. Thanks to improved accuracy and physical consistency, this formulation enables realistic predictions of the reduced explosion pressure, thus offering engineers and designers a robust basis for sizing vent areas, selecting structural reinforcements, and ensuring the safe design of explosion relief systems in filter-equipped collectors.

Nonetheless, the model has defined applicability limits that should be acknowledged. Congestion ratios beyond 0.60 were not analyzed, as commercial dust collectors rarely exceed this threshold. Both simulations and test data suggest that pressure levels approach a plateau beyond this point, reducing the practical benefit of further extrapolation.

Furthermore, highly reactive dusts with $K_{St} > 30$ MPa m/s were not included in the regression due to limited data. Although the model remains well-behaved in this regime, its accuracy under these conditions remains to be verified.

In conclusion, the proposed correlation provides a practical, data-anchored tool that measurably improves current venting approaches for dust collectors. By explicitly accounting for internal congestion through a logarithmic factor, it reduces the systematic underestimation of reduced pressure that can occur when applying empty-vessel or weakly congestion-sensitive relations. Within its calibrated range, it delivers tighter agreement with full-scale measurements and, consequently, more reliable estimates of peak blast loads. This enables structural designers to size vent areas and anchorage greater safety margins and fewer non-conservative outcomes. We acknowledge defined limits of applicability and the need for broader datasets, nonetheless, for the configurations considered, the correlation achieves its purpose: improving the safety and predictiveness of maximum pressure estimates for dust-collector deflagrations.

Future work should expand experimental datasets and extend the formulation to include ducted vents and higher-reactivity dust, further consolidating the model's applicability in industrial safety engineering. Particular attention should also be given to the influence of vessel aspect ratio (L/D), which has been shown to significantly affect flame propagation dynamics and pressure piling in interconnected systems (Ogungbemide et al., 2021; Ren et al., 2025), as well as to the explosion behavior of hybrid mixtures, which may introduce synergistic effects not predictable from single-fuel data (Schrader et al., 2025).

CRediT authorship contribution statement

F. Pinna: Writing – review & editing, Writing – original draft, Visualization, Validation, Software, Methodology, Investigation, Formal analysis. **M. Zucca:** Writing – review & editing, Project administration. **M. Simoncelli:** Writing – review & editing, Project administration, Funding acquisition. **F. Stochino:** Writing – review & editing, Validation, Supervision, Resources, Project administration, Methodology, Funding acquisition.

Funding sources

This work was supported by METAL WORKING S.r.l. [Project name: MW 24].

Declaration of competing interest

The authors declare no conflict of interest for the manuscript entitled "A New Logarithmic Congestion Model for Vent Sizing and Reduced Pressure Prediction in Baghouse Dust Collectors".

Acknowledgements

The authors wish to thank Alessandro Gardumi for his valuable support.

Data availability

Data will be made available on request.

References

Abbasi, T., Abbasi, S.A., 2007. Dust explosions–Cases, causes, consequences, and control. J. Hazard Mater. 140 (1–2), 7–44.

Alauddin, M., Addo, A., Khan, F., Amyotte, P., 2025. Probabilistic modeling of explosibility of low reactivity dusts. Reliab. Eng. Syst. Saf., 110861 https://doi.org/10.1016/j.ress.2025.110861.

American Society for Testing and Materials (ASTM), 2020. ASTM E1226: Standard Test Method for Explosibility of Dust Clouds. ASTM. Retrieved from. https://www.astm.org/e1226-19.html.

Amyotte, P.R., Chippett, S., Pegg, M.J., 1988. Effects of turbulence on dust explosions. Prog. Energy Combust. Sci. 14 (4), 293–310. https://doi.org/10.1016/0360-1285(88)90016-0.

Arntzen, B.J., Lucas, M., Ghaffari, M., 2025. An Arrhenius reaction rate based burning model for simulation of dust explosions. J. Loss Prev. Process. Ind., 105638 https://doi.org/10.1016/j.jlp.2025.105638.

Bartknecht, W., 1978. Gas, vapour and dust explosions: fundamentals, prevention, control. In: Ciba-Geigy Limited. Contribution Prepared for the *International Symposium on Grain Elevator Explosions*, Organized by the *US*. National Research Council, Washington, D.C.. July 11–12, 1978. https://nap.nationalacademies.org/read/20025/chapter/7#56

Bartknecht, W., 1981. Explosions-Course, Prevention, Protection.

Bauwens, C.R., Chaffee, J., Dorofeev, S., 2010. Effect of ignition location, vent size, and obstacles on vented explosion overpressures in propane-air mixtures. Combust. Sci. Technol. 182 (11–12), 1915–1932. https://doi.org/10.1080/00102202.2010.497415.

Bradley, D., Lawes, M., Liu, K., Mansour, M.S., 2013. Measurements and correlations of turbulent burning velocities over wide ranges of fuels and elevated pressures. Proc. Combust. Inst. 34 (1), 1519–1526.

Cashdollar, K.L., 2000. Overview of dust explosibility characteristics. J. Loss Prev. Process. Ind. 13 (3–5), 183–199. https://doi.org/10.1016/S0950-4230(99)00039-X.

European Committee for Standardization (CEN), 2012. EN 14491: Dust Explosion Venting Protective Systems. CEN. Retrieved from. https://store.uni.com/uni-en-14491-2012.

Eckhoff, R.K., 2003. Dust Explosions in the Process Industries: Identification, Assessment and Control of Dust Hazards. elsevier.

Fritsch, F.N., Carlson, R.E., 1980. Monotone piecewise cubic interpolation. SIAM J. Numer. Anal. 17 (2), 238–246.

Guan, L., Zhao, F., Lu, Q., Zhang, D., Zhu, B., Wang, Y., 2025. Centrifuge modeling of dynamic response of underground concrete silo against adjacent buried explosion loads. Int. J. Impact Eng. 200, 105256. https://doi.org/10.1016/j.ijimpeng.2025.105256.

Hassan, J., Khan, F., Amyotte, P., Ferdous, R., 2014. A model to assess dust explosion occurrence probability. J. Hazard Mater. 268, 140–149. https://doi.org/10.1016/j.jhazmat.2014.01.017.

Hansen, O.R., Gavelli, F., Ichard, M., Davis, S.G., 2010a. Validation of FLACS against experimental data sets from the model evaluation database for LNG vapor dispersion. J. Loss Prev. Process. Ind. 23 (6), 857–877. https://doi.org/10.1016/j.jlp.2010.08.005.

Hansen, O.R., Hinze, P., Engel, D., Davis, S., 2010b. Using computational fluid dynamics (CFD) for blast wave predictions. J. Loss Prev. Process. Ind. 23 (6), 885–906. https://doi.org/10.1016/j.jlp.2010.07.005.

Islas, A., Portarapillo, M., Pandal, A., Sanchirico, R., Di Benedetto, A., 2025. CFD model of dust unsteady flame propagation in the 20 L bomb. J. Loss Prev. Process. Ind. 94, 105573. https://doi.org/10.1016/j.jlp.2025.105573.

Li, J., Hao, H., 2017. Internal and external pressure prediction of vented gas explosion in large rooms by using analytical and CFD methods. J. Loss Prev. Process. Ind. 49, 367–381. https://doi.org/10.1016/j.jlp.2017.08.002.

Li, X., Chen, H., Zhang, Y., Zhang, X., Li, R., 2022. Research on law and mechanism of dust explosion in bag type dust collector. Adv. Powder Technol. 33 (6), 103619. https://doi.org/10.1016/j.apt.2022.103619.

Li, Q., Wang, Y., Shao, Y., Li, L., Hao, H., 2023. A comparative study on the most effective machine learning model for blast loading prediction: from GBDT to transformer. Eng. Struct. 276, 115310. https://doi.org/10.1016/j.engstruct.2022.115310.

Li, S., Gao, K., Xia, H., Yang, Y., Wang, X., 2024. Effect of low blockage ratio obstacle on explosion characteristic in methane/air mixture. Arab. J. Chem. 17 (9), 105890. https://doi.org/10.1016/j.arabjc.2024.105890.

Li, Q., Li, L., Shao, Y., Wang, R., Hao, H., 2025. A multi-task machine learning approach for data efficient prediction of blast loading. Eng. Struct. 326, 119577. https://doi.org/10.1016/j.engstruct.2024.119577.

Lyu, X., Qiao, Y., Yuan, D., Zhang, Z., Zuo, W., Hua, J., et al., 2024. Investigation and CFD simulation of coal dust explosion accident in confined space: a case study of gaohe coal mine ventilation air methane oxidation power plant. Fire Saf. J. 149, 104237.

Luersen, M.A., Le Riche, R., 2004. Globalized Nelder–Mead method for engineering optimization. Comput. Struct. 82 (23–26), 2251–2260. https://doi.org/10.1016/j.compstruc.2004.03.072.

Lunn, G.A., Cairns, F., 1985. The venting of dust explosions in a dust collector. J. Hazard Mater. 12 (1), 87–107. https://doi.org/10.1016/0304-3894(85)80027-3.

Lunn, G.A., Nicol, A.M., Collins, P.D., Hubbard, N.R., 1998. Effects of vent ducts on the reduced pressures from explosions in dust collectors. J. Loss Prev. Process. Ind. 11 (2), 109–121. https://doi.org/10.1016/S0950-4230(97)00036-3.

Ma, G., Li, J., Abdel-jawad, M., 2014. Accuracy improvement in evaluation of gas explosion overpressures in congestions with safety gaps. J. Loss Prev. Process. Ind. 32, 358–366. https://doi.org/10.1016/j.jlp.2014.10.007.

Marmo, L., Portarapillo, M., Di Benedetto, A., Sanchirico, R., Danzi, E., 2025. Dust explosion risk in polymer powder processing: review and testing. J. Loss Prev. Process. Ind. 94, 105528. https://doi.org/10.1016/j.jlp.2024.105528.

Nan, F., Cheng, F.M., Luo, Z.M., Wang, J.Y., Chen, X.K., Xiao, Y., 2023. Characteristics of dust explosion venting pressure and flame under high activation pressure. J. Loss Prev. Process. Ind. 84, 105108. https://doi.org/10.1016/j.jlp.2023.105108.

National Fire Protection Association (NFPA), 2023. NFPA 68: Standard on Explosion Protection by Deflagration Venting. NFPA. Retrieved from. https://link.nfpa.org/publications/68/2023/.

Ogungbemide, D., Clouthier, M.P., Cloney, C., Zalosh, R.G., Ripley, R.C., Amyotte, P.R., 2021. Numerical modelling of the effects of vessel length-to-diameter ratio (L/D) on pressure piling. J. Loss Prev. Process. Ind. 70, 104398. https://doi.org/10.1016/j.jlp.2021.104398.

Paltrinieri, N., Khan, F., Amyotte, P., Cozzani, V., 2014. Dynamic approach to risk management: application to the Hoeganaes metal dust accidents. Process Saf. Environ. Prot. 92 (6), 669–679. https://doi.org/10.1016/j.psep.2013.11.008.

Pang, L., Li, W., Zhang, Z., Sun, S., Yang, K., 2023. Influence of vent duct bend angle on inner dust explosion. J. Loss Prev. Process. Ind. 85, 105173. https://doi.org/10.1016/j.jlp.2023.105173.

Pang, L., Cao, J., Xiao, Q., Yang, K., Shi, L., 2022. Explosion propagation in a dust removal pipeline under dust collector explosion. J. Loss Prev. Process. Ind. 74, 104662. https://doi.org/10.1016/j.jlp.2021.104662.

Pang, L., Liu, J., 2024. Research on the explosion vent external composite disaster induced by dust explosion inside the dust collector. J. Loss Prev. Process. Ind. 91, 105376. https://doi.org/10.1016/j.jlp.2024.105376.

Park, D.J., Lee, Y.S., Green, A.R., 2008. Prediction for vented explosions in chambers with multiple obstacles. J. Hazard Mater. 155 (1–2), 183–192. https://doi.org/10.1016/j.jhazmat.2007.11.052.

Peters, N., 2001. Turbulent combustion. Meas. Sci. Technol. 12 (11), 2022. https://doi.org/10.1088/0957-0233/12/11/708, 2022.

Phylaktou, H., Andrews, G.E., Liu, Y., 1994. Turbulent explosions: a study of the influence of the obstacle scale. In: INSTITUTION OF CHEMICAL ENGINEERS SYMPOSIUM SERIES, vol. 134. HEMSPHERE PUBLISHING CORPORATION, p. 269, 269.

Pinna, F., Zucca, M., Simoncelli, M., Stochino, F., 2025. Explosion venting in dust collectors: a critical review of standards for reduced pressure and reaction force duration. J. Loss Prev. Process. Ind., 105670 https://doi.org/10.1016/j.jlp.2025.105670.

Ren, J., Bai, C., Zhao, X., Zeng, L., Wang, Z., 2025. Research on the evolution of state field and damage range of multiple source cloud explosions. Int. J. Impact Eng. 196, 105182. https://doi.org/10.1016/j.ijimpeng.2024.105182.

Robert, H.P., Don, W.G., James, O.M., 1984. Perry's Chemical Engineer's Handbook. Nova Iorque.

Schafer, R.W., 2011. What is a savitzky-golay filter?[lecture notes]. IEEE Signal Process. Mag. 28 (4), 111–117.

Schrader, A., Axani, K., Alauddin, M., Scott, A., Cloney, C., Amyotte, P., 2025. Hybrid mixture explosions in an industrial polymer production process. J. Loss Prev. Process. Ind. 96, 105646. https://doi.org/10.1016/j.jlp.2025.105646.

Skjold, T., Arntzen, B.J., Hansen, O.R., Taraldset, O.J., Storvik, I.E., Eckhoff, R.K., 2005. Simulating dust explosions with the first version of DESC. Process Saf. Environ. Prot. 83 (2), 151–160. https://doi.org/10.1205/psep.04237.

Skjold, T., 2007. Review of the DESC project. J. Loss Prev. Process. Ind. 20 (4–6), 291–302. https://doi.org/10.1016/j.firesaf.2024.104237.

Skjold, T., 2018. Dust explosion modeling: status and prospects. Part. Sci. Technol. 36 (4), 489–500. https://doi.org/10.1080/02726351.2017.1389790.

Tascón, A., Aguado, P.J., 2017. Simulations of vented dust explosions in a 5 m3 vessel. Powder Technol. 321, 409–418. https://doi.org/10.1016/j.powtec.2017.08.047.

U.S. Chemical Safety and Hazard Investigation Board, 2018. Dust Incidents 2006–2017. U.S. Chemical Safety Board. Retrieved from. https://www.csb.gov.

Verein Deutsher Ingenieurteg (VDI), 2002. VDI 3673 Blatt 1: Druckentlastung von Staubexplosionen. Retrivied from. https://www.vdi.de/en/home/vdi-standards/details/vdi-3673-blatt1-pressure-venting-of-dust-explosions.

Wu, Q., Yu, M., Zheng, K., 2022. Experimental investigation on the effect of obstacle position on the explosion behaviors of the non-uniform methane/air mixture. Fuel 320, 123989. https://doi.org/10.1016/j.fuel.2022.123989.

Xie, F., Wang, Z., Guo, S., Pan, X., Jiang, J., 2025. CFD simulation of turbulent diffusion and phase transition of methanol spray in a 20L spherical vessel. J. Loss Prev. Process. Ind., 105656 https://doi.org/10.1016/j.jlp.2025.105656.

Xu, H., Wang, X., Li, Y., Zhu, P., Cong, H., Qin, W., 2017. Experimental investigation of methane/coal dust explosion under influence of obstacles and ultrafine water mist. J. Loss Prev. Process. Ind. 49, 929–937. https://doi.org/10.1016/j.jlp.2017.04.016.

Yin, S., Dai, H., Chen, X., Wang, Y., Zhao, Q., Wang, X., et al., 2019. Effect of obstacles on flame propagation characteristics of corn starch dust. Combust. Sci. Technol. 191 (11), 2006–2019. https://doi.org/10.1080/00102202.2018.1542380.

Zahara, E., Kao, Y.T., 2009. Hybrid Nelder–Mead simplex search and particle swarm optimization for constrained engineering design problems. Expert Syst. Appl. 36 (2), 3880–3886. https://doi.org/10.1016/j.eswa.2008.02.039.

Zhang, Q., Wang, Y., Lian, Z., 2017. Explosion hazards of LPG-air mixtures in vented enclosure with obstacles. J. Hazard Mater. 334, 59–67. https://doi.org/10.1016/j.jhazmat.2017.03.065.

Zhang, S., Yan, X., Wen, Z., Meng, S., Lu, Y., Shi, S., 2024. Study on the explosion mechanism of two-phase organic dust—Based on polypropylene/propylene hybrid explosions as an example. J. Loss Prev. Process. Ind. 92, 105429. https://doi.org/10.1016/j.jlp.2024.105429.

Zhang, L., Luo, Z., Su, B., Song, Z., Deng, J., Ji, X., 2025. Prediction of explosion hazard of aluminum powder two-phase mixed system using random forest based on K-fold cross-validation. J. Loss Prev. Process. Ind. 94, 105574. https://doi.org/10.1016/j.jlp.2025.105574.

Zhou, Z., Wang, G., Xu, J., Wang, H., Zhang, L., Liu, Y., 2024. Influence of the shape and number of obstacles on the excitation effect of dust-containing gas explosion. Powder Technol. 448, 120253. https://doi.org/10.1016/j.powtec.2024.120253.